

# A hidden Markov model reliably characterizes ketamine-induced spectral dynamics in macaque LFP and human EEG

Indie C. Garwood<sup>#, 1,2,3</sup>, Sourish Chakravarty<sup>#, 2, 4</sup>, Jacob Donoghue<sup>1,2,3</sup>, Pegah Kahali<sup>4,2</sup>, Shubham Chamadia<sup>4</sup>, Oluwaseun Akeju<sup>4</sup>, Earl K. Miller<sup>2,3</sup>, and Emery N. Brown<sup>\*, 1,2,3,4</sup>

<sup>1</sup>Harvard-MIT Division of Health Sciences and Technology, MIT, Cambridge, MA;

<sup>2</sup>The Picower Institute for Learning and Memory, Massachusetts Institute of Technology (MIT), Cambridge, MA;

<sup>3</sup>Department of Brain and Cognitive Sciences, MIT, Cambridge, MA;

<sup>4</sup>Department of Anesthesia, Critical Care, and Pain Medicine, Massachusetts General Hospital, Boston, MA;

<sup>#</sup>Co-first Authors

<sup>\*</sup>Corresponding Author. Email: [enb@neurostat.mit.edu](mailto:enb@neurostat.mit.edu)

October 19, 2020

## Abstract

Ketamine is an NMDA receptor antagonist commonly used to maintain general anesthesia. At anesthetic doses, ketamine causes bursts of 30-50 Hz oscillations alternating with 0.1 to 10 Hz oscillations. These dynamics are readily observed in local field potentials (LFPs) of non-human primates (NHPs) and electroencephalogram (EEG) recordings from human subjects. However, a detailed statistical analysis of these dynamics has not been reported. We characterize ketamine's neural dynamics using a hidden Markov model (HMM). The HMM observations are sequences of spectral power in 10 Hz frequency bands between 0 to 50 Hz, where power is averaged within each band and scaled between 0 and 1. We model the observations as realizations of multivariate beta probability distributions that depend on a discrete-valued latent state process whose state transitions obey Markov dynamics. Using an expectation-maximization algorithm, we fit this beta-HMM to LFP recordings from 2 NHPs, and separately, to EEG recordings from 9 human subjects who received anesthetic doses of ketamine. Together, the estimated beta-HMM parameters and optimal state trajectory revealed an alternating pattern of states characterized primarily by gamma burst and slow oscillation activity, as well as intermediate states in between. The mean duration of the gamma burst state was 2.5s([1.9,3.4]s) and 1.2s([0.9,1.5]s) for the two NHPs, and 2.7s([1.9,3.8]s) for the human subjects. The mean duration of the slow oscillation state was 1.6s([1.1,2.5]s) and 0.7s([0.6,0.9]s) for the two NHPs, and 2.8s([1.9,4.3]s) for the human subjects. Our beta-HMM framework provides a useful tool for experimental data analysis. Our characterizations of the gamma-burst process offer detailed, quantitative constraints that can inform the development of rhythm-generating neuronal circuit models that give mechanistic insights into this phenomenon and how ketamine produces altered states of arousal.

35 **Keywords:** Ketamine, Anesthesia, Unconsciousness, EEG, Local Field Potential, Non-human primates,  
36 Prefrontal cortex, Hidden Markov Model, Beta distribution, Multitaper spectra, Reduced-order modeling.

## 37 1 Introduction

38 Ketamine is a phenylcyclidine derivative and one of the most commonly used anesthetics in clinical use world-  
39 wide [1, 2, 3, 4]. It is classified as a WHO Essential Medicine [5], and is often the only anesthetic available  
40 in clinics of developing countries [6]. At low doses, ketamine is known to create a state of “dissociative  
41 anesthesia” characterized by altered sensory perception and analgesia [1, 2]. At high doses it also leads  
42 to loss of consciousness, and therefore it is often used as an anesthetic agent during surgery in humans  
43 and animals [3, 7, 8, 9]. Under anesthetic dosages, ketamine produces distinct oscillatory signatures in the  
44 electroencephalogram (EEG) of healthy volunteers and patients [10, 11, 12]. In a recent retrospective study  
45 by Akeju et al. [11], the authors found that the frontal EEG from patients who received ketamine for the  
46 induction of general anesthesia showed distinct alternating periods of intermittent high power activity in the  
47 27 – 40 Hz and 0.1 – 4 Hz frequency bands. Spontaneous gamma oscillations (i.e. 30 – 50 Hz) have also  
48 been demonstrated under ketamine-induced general anesthesia in mice [13], non-human primates (NHPs)  
49 [14, 15, 16], and sheep [17]. Recent neuroscience research in NHPs under high-dose ketamine, revealed  
50 prominent gamma oscillations modulated by slow wave (0.3 Hz) activity [16], similar to the alternating  
51 bursts of activity in gamma and slow-delta bands observed in humans [11]. Objective characterization of  
52 the intermittent band-limited spectral dynamics induced by ketamine would be useful both for monitoring  
53 patients during ketamine-induced unconsciousness in clinical settings, as well as for aiding computational  
54 and experimental neuroscience research aimed at building a mechanistic understanding of the phenomena.  
55 Therefore, the availability of an efficient analytic tool, which can objectively detect and characterize ketamine-  
56 induced transient neural dynamics, can catalyze both clinical and neuroscience innovations.

57 Ketamine’s primary pharmacologic effect is N-Methyl-d-aspartate (NMDA) receptor antagonism. One  
58 putative mechanism of ketamine induced cortical gamma oscillations is that ketamine preferentially blocks  
59 NMDA receptors on fast spiking inhibitory gamma aminobutyric acid (GABA) interneurons. The blocking  
60 of the NMDA receptors on the interneurons results in reduced interneuron activity, and a reduction of  
61 GABA release at the synapse between interneurons and excitatory pyramidal neurons. The reduction of  
62 GABA causes disinhibition of the pyramidal neurons, resulting in increased pyramidal neuron activity that  
63 manifests as cortical gamma oscillations [18, 19]. This mechanism, however, does not explain the presence  
64 of periodic bursts of gamma activity. A recent modeling study suggests a cyclic mechanism where in each  
65 cycle, the pyramidal neurons that are disinhibited at the beginning of the cycle provide sufficient input to  
66 the interneurons for the latter to overcome the ketamine inhibition and release GABA, which then results in  
67 temporary inhibition of the pyramidal neurons towards the end of the cycle [20]. A statistical characterization  
68 of the ketamine-induced alternating gamma burst and slow-oscillation activity in neural data can provide  
69 informative quantitative constraints for mechanistic neuronal circuit models of ketamine-induced spectral  
70 dynamics. Such mechanistic models can further aid the understanding of how ketamine causes altered  
71 states of arousal. Examples of how detailed statistical analyses of neural data has guided neurophysiological  
72 modeling studies can be found in existing works that studied propofol-induced unconsciousness [21, 22, 23,  
73 24].

74 State-space models provide a versatile statistical framework for analyzing the dynamics of complex neural  
75 time-series data [25]. These models have been widely used in neuroscience, from decoding hippocampal

76 place cells [26], to tracking movement intention in the motor cortex [27, 28, 29], to assessing the level of  
77 unconsciousness in medically-induced coma [30]. A particular class of state-space models, known as Hidden  
78 Markov Models (HMMs), have been used to describe underlying dynamical processes driven by stochastic  
79 switching between discrete states, where each state is associated with a distinct observation probability  
80 distribution [31, 32, 33, 34, 35, 36]. HMMs have been used to objectively decode neurophysiological states,  
81 including detecting seizure events [37], classifying sleep stages [38, 39, 40, 41], decoding speech [42, 43], and  
82 decoding movement intention [44, 45]. HMMs have also been used to provide detailed statistical descriptions  
83 of neural phenomena [46, 47, 48]. Since ketamine-induced cortical activity is characterized by distinct  
84 switching patterns in oscillatory dynamics, an HMM is a plausible statistical model for both estimating  
85 neurophysiological states and characterizing their statistical properties. Our preliminary analysis using an  
86 HMM to characterize ketamine-induced spectral dynamics in human EEG and in local field potential (LFP)  
87 from NHPs yielded promising results [49]. Along similar lines, the recent work by Li and Mashour [12], using  
88 a particular class of HMMs [50] to characterize multichannel scalp EEG from healthy volunteers, further  
89 supports the utility of HMMs to analyze ketamine spectra. By inferring an HMM from neural activity  
90 spectra, we can quantitatively characterize the discontinuous spectral dynamics in terms of the parameters  
91 of the best-fitting observation and state transition models, as well as the state trajectory corresponding to  
92 the entire data sequence.

93 In this work, we develop an HMM-based analysis framework to characterize ketamine-induced spectral  
94 dynamics recorded in neurophysiological data from 2 NHPs and 9 human subjects in the operating room  
95 (see schema in Fig. 1). The observations that go into our HMM analysis are sequences of spectral power in  
96 10 Hz frequency bands between 0 and 50 Hz. The power is averaged within each band and scaled between 0  
97 and 1 to facilitate comparison among data sets that vary in power amplitude but not in the spectral profiles  
98 they represent. To describe this multivariate observation sequence, we assume that the spectral dynamics  
99 are governed by a discrete-valued latent state process, where each state corresponds to a distinct spectral  
100 profile. We model these spectral profiles as realizations of state-specific and frequency-band specific beta  
101 distributions. From the estimated HMM, we are able to objectively characterize the dynamic evolution of  
102 neurophysiological states induced by ketamine. By applying this tool to analyze neural data from both  
103 NHPs and humans, we obtain precise estimates of time-scales associated with neurophysiological phenomena  
104 observed in both species (e.g., alternating gamma-slow activity).

105 The paper is organized as follows. In the following section 2 we present our beta-HMM formulation,  
106 corresponding estimation framework, and useful statistics based on the estimated beta-HMM. In section 3  
107 we describe the electrophysiology datasets to which we apply our analysis framework. We present the results  
108 from our beta-HMM analyses in section 4. Finally, in section 5 we summarize the core contribution of our  
109 work, highlight the connections between our work and that of others, and suggest next steps.

## 110 2 A hidden Markov model for beta distributed observations

### 111 2.1 Reduced-order observations derived from multitaper spectrogram

112 We consider a sequence of scalar-valued single-channel voltage activity representing either LFP or EEG  
113 sampled at frequency  $F_s$  (in Hz). To quantify the spectral dynamics in the signal, we estimate time-  
114 varying spectra across a sequence of overlapping time-windows, each of duration  $\Delta_{MT} = 1s$ , with 90%  
115 overlap between consecutive windows. The power spectral density (in dB) at the  $n$ -th time-window and

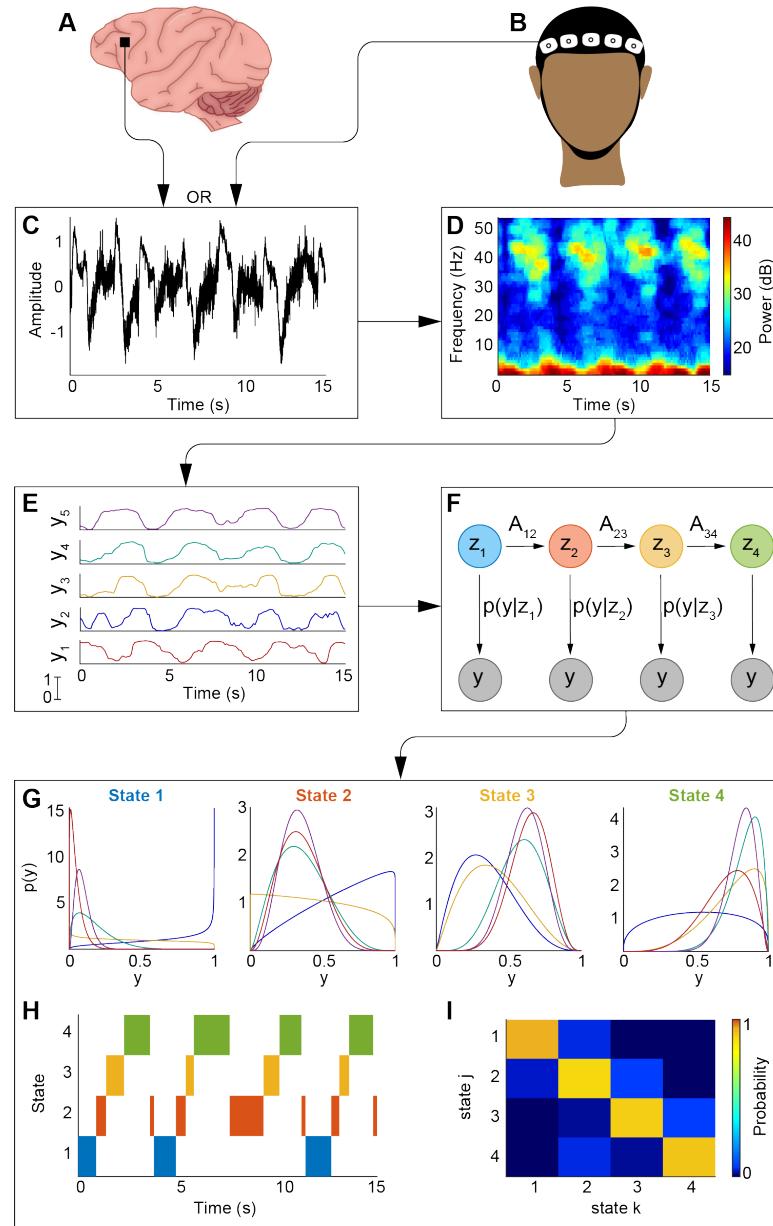


Figure 1: **Schematic of the beta-HMM algorithm.** Neural recordings from primate LFP (A) or human EEG (B) serve as inputs to the algorithm. Electrical recordings (C) are converted to their time-frequency representation via multitaper spectral analysis (D). The spectral observations are split into 10 Hz frequency bands and scaled between 0 and 1 (E). These observations are then fit to the beta-HMM (F) via the EM algorithm, and the state trajectory is estimated from the Viterbi algorithm. Outputs of the algorithm are the beta observation distributions for each state (G), estimated state trajectory (H), and a transition matrix (I) describing the state switching dynamics.

Table 1: Glossary of mathematical symbols.

$F_s$	Sampling frequency (in Hz)
$\Delta_{MT}$	Length of the time-window (in seconds) over which the signal is assumed to be second order stationary.
$S_n(\omega_i)$	Power spectral density (in dB) corresponding to frequency $\omega_i$ (in Hz) at the $n$ -th time-window.
$\omega_r$	Frequency resolution (in Hz) at which the multitaper spectral estimates are calculated.
$\bar{S}_n(\omega_h)$	Average power spectral density for the $h$ -th frequency band. Note: we use the symbol $\omega$ to indicate both frequency and frequency-band. The context makes the distinction clear.
$H$	Number (num.) of frequency bands.
$N$	Num. of time-points where spectral estimates are available from a neural (LFP or EEG) recording session.
$\omega$	$= \{\omega_h\}_{h=1}^H$ , the set of all frequency bands,
$\bar{\mathbf{S}}(\omega_h)$	$= \{\bar{S}_n(\omega_h)\}_{n=1}^N$ , vector of $N$ average spectral densities for the frequency band $\omega_h$ .
$Q_j(\bar{\mathbf{S}}(\omega_h))$	The $j$ -th quartile of the sequence $\bar{\mathbf{S}}(\omega_h)$
$\mathbf{y}_n$	Vector (of size $H \times 1$ ) scaled power values corresponding to the $n$ -th time-point.
$\mathbf{y}_h$	Vector (of size $N \times 1$ ) scaled power values corresponding to the $h$ -th frequency band.
$y_{nh}$	The $h$ -th element of $\mathbf{y}_n$ taking real values in the range $[0,1]$ .
$\lambda_h$	A user-defined parameter used in scaling the spectral power values in the $h$ -th frequency band to a value in the range $[0, 1]$ .
$K$	Num. of latent states in a HMM.
$z_n$	Discrete-valued random variable denoting the latent state at the $n$ -th timepoint. $z_n \in [1, K]$ .
$p(x)$	The value that the probability density function (pdf) takes at a sample point $x$ of a continuous-valued random variable. The corresponding probability space is implied [51].
$\mathcal{B}(a, b)$	The beta function taking arguments $a$ and $b$ .
$a_{hk}, b_{hk}$	The parameters of the beta pdf corresponding to the $k$ -th latent state and $h$ -th frequency band.
$\phi_k$	The set of beta pdf parameters corresponding to the $k$ -th latent state and all the $H$ frequency bands $= \{a_{hk}, b_{hk}\}_{h=1}^H$ .
$\phi$	The set of all beta pdf parameters corresponding to all the $K$ latent states and all the $H$ frequency bands $= \{\phi_k\}_{k=1}^K$ .
$Pr(\cdot)$	This indicates the probability measure that maps an element in the event space (corresponding to a random variable) to a value in the interval $[0, 1]$ [51].
$A_{jk}$	Probability to transition to state $z_n = k$ from a previous state $z_{n-1} = j$ for any $n \in [2, N]$ .
$\mathbf{A}$	The $K \times K$ state transition matrix whose element in the $j$ -th row and $k$ -th column is $A_{jk}$ .
$\pi_k$	Probability of the occurrence $z_1 = k$ where $z_1$ indicates the initial state of a Markov path.
$\boldsymbol{\pi}$	$= \{\pi_k\}_{k=1}^K$ , the vector of initial state probabilities
$L$	Num. of statistically independent recording sessions that a model will be fitted to.
$\mathbf{y}_{n,l}$	The observation vector at the $n$ -th time-point of the $l$ -th recording session.
$N_l$	Num. of time-points where spectral estimates are available from the $l$ -th neural recording session.
$\mathbf{Y}_l$	$= \{\mathbf{y}_{n,l}\}_{n=1}^{N_l}$ , the set of all scaled powers from the $l$ -th neural recording session.
$\boldsymbol{\pi}_l$	The initial state probability vector for the $l$ -th recording session.
$\Theta$	Set of all model parameters, $\{\{\boldsymbol{\pi}_l\}_{l=1}^L, \mathbf{A}, \phi\}$ , of a HMM describing the observations in $L$ independent recording sessions.
$z_{n,l}$	The latent state at the $n$ -th time-point of the $l$ -th session.
$\mathbf{Z}_l$	$= \{z_{n,l}\}_{n=1}^{N_l}$ , the set of $N_l$ latent states denoting the latent state trajectory for the $l$ -th session .
$Q(\Theta, \hat{\Theta})$	The expectation of the complete data log-likelihood function (parameterized by $\Theta$ ) where the expectation operation is over latent state trajectories, $\mathbf{Z}_1, \dots, \mathbf{Z}_L$ , that are estimated using an HMM with parameters $\hat{\Theta}$ .
$\gamma_{n,l}(k)$	$= Pr(z_{n,l} = k   \mathbf{Y}_l, \boldsymbol{\pi}, \mathbf{A}, \phi)$ , the posterior probability of the occurrence of $z_{n,l} = k$ given the observations from the $l$ -th session ( $\mathbf{Y}_l$ ) and model parameters ( $\boldsymbol{\pi}, \mathbf{A}$ and $\phi$ ).
$\xi_{n,l}(j, k)$	$= Pr(z_{n-1,l} = j, z_{n,l} = k   \mathbf{Y}_l, \boldsymbol{\pi}, \mathbf{A}, \phi)$ , the posterior probability of the joint occurrence of $z_{n-1,l} = j$ and $z_{n,l} = k$ given the observations from the $l$ -th session ( $\mathbf{Y}_l$ ) and model parameters ( $\boldsymbol{\pi}, \mathbf{A}, \phi$ ).
$(Y_h   Z = k)$	Scalar-valued random variable indicating the scaled power $Y_h$ in the $h$ -th frequency band conditioning on the discrete-valued random variable $Z$ , indicating the latent state, at $k$ .
$\Delta_{hj}$	A random variable denoting the difference between two scalar-valued continuous random variables as such, $X_{hj} - X_{hk}$ , where $X_{hj} \sim Beta(a_{hj}, b_{hj})$ and $X_{hk} \sim Beta(a_{hk}, b_{hk})$ .

116 corresponding to frequency  $\omega_i$  (in Hz) is denoted by  $S_n(\omega_i)$ . We use the multitaper spectral estimation  
 117 approach [52, 53, 54] (time-halfbandwidth product = 2, and number of tapers = 3) to calculate the sequence  
 118  $\{S_n(\omega_i)\}_{n=1}^N$  on a high dimensional set of distinct frequencies  $\{\omega_i : 0 < \omega_i < F_s/2\}$ . We reduce the complexity  
 119 of our subsequent analyses by summarizing the high-dimensional information  $S_n(\{\omega_i\})$  by a low-dimensional  
 120 vector  $\bar{S}_n(\{\omega_h\})$ . This low-dimensional vector characterizes the instantaneous average power in  $H$  ( $= 5$ )  
 121 distinct 10 Hz frequency bands between 0-50 Hz, such that

$$122 \quad \bar{S}_n(\omega_h) = \frac{\omega_r}{10} \sum_{i=10\omega_r^{-1}(h-1)+1}^{10\omega_r^{-1}h} S_n(\omega_i), \quad \text{where } h \in \{1, 2, \dots, H\}, \quad (1)$$

124 and  $\omega_r$  denotes the frequency resolution of the multitaper spectral estimates. The choice of the frequency  
 125 bands was based on our initial observation that in both NHP LFP and human EEG, significant dynamic  
 126 activity across  $\{S_n(\omega_i)\}_{n=1}^N$  occurred in 0 – 50 Hz during ketamine induction [49]. This range encompasses  
 127 the frequencies considered in previous studies of ketamine-induced changes in EEG spectra in healthy human  
 128 subjects and patients [11, 12]. The sequence  $\bar{S}_n(\boldsymbol{\omega})$  where,  $\boldsymbol{\omega} = \{\omega_h\}_{h=1}^H$ , is input to the beta-HMM analysis  
 129 <sup>1</sup>.

## 130 2.2 Observation model

131 To facilitate the comparison of spectral observations across different data sets whose spectral power may  
 132 vary in amplitude but represent comparable spectral profiles, we scale  $\bar{S}_n(\boldsymbol{\omega})$  to new vector  $\mathbf{y}_n \in [0, 1]^H$   
 133 whose  $h$ -th element is calculated as,

$$134 \quad y_{nh} = \frac{1}{1 + e^{-\lambda_h(\bar{S}_n(\omega_h) - Q_2(\bar{\mathbf{S}}(\omega_h)))}} \quad , \text{ for } h \in \{1, \dots, H\}, \quad (2)$$

136 where,  $Q_j(\bar{\mathbf{S}}(\omega_h))$  denotes the function that operates on a real-valued sequence  $\bar{\mathbf{S}}(\omega_h) = \{\bar{S}_n(\omega_h)\}_{n=1}^N$  to  
 137 yield the  $j$ -th quartile. The user-defined parameter  $\lambda_h$  controls the mutual separation of points in the  
 138  $y_{nh}$ -space relative to their corresponding map in the  $\bar{S}_n(\omega_h)$ -space. We set this value to be  $\lambda_h = 2 \log(3)/$   
 139  $(Q_3(\bar{\mathbf{S}}(\omega_h)) - Q_1(\bar{\mathbf{S}}(\omega_h)))$ . The intuition behind this choice is that it results in scaling of the data between  
 140 the 1st and 3rd quartiles approximately linearly between [0.25, 0.75]. Data below the 1st quartile and beyond  
 141 the 3rd quartile are scaled non-linearly, such that very small values are scaled to be close to zero and very  
 142 large values are scaled to be close to one. Compared to linear 0-1 scaling, the logistic scaling method is  
 143 less sensitive to outliers which, in linear scaling, can lead to low variance observations and thus reduce the  
 144 likelihood of detecting distinct spectral profiles. With logistic scaling, the data in  $\bar{\mathbf{S}}(\omega_h)$  is scaled such that  
 145 the standard deviations of the observations in each frequency band ( $\mathbf{y}_h$ ) are between [0.22, 0.30] for all data  
 146 sets reported here.

147 In our model, we assume that for the  $n$ -th time-window, the observation  $\mathbf{y}_n$  is a manifestation of an  
 148 underlying latent brain state,  $z_n$ , at the same instant. We also assume that  $z_n$  is a random process that  
 149 transitions among  $K$  possible discrete states, each with its own characteristic observation probability distri-  
 150 bution whose mean corresponds to a distinct spectral profile. We represent a state-specific and frequency

<sup>1</sup>We use bold math symbols to indicate vector-valued quantities.

151 band-specific probability density function (pdf) of the observations as a standard beta distribution:

$$152 \quad p(y_{nh}|z_n = k; a_{hk}, b_{hk}) = \frac{y_{nh}^{a_{hk}-1}(1-y_{nh})^{b_{hk}-1}}{\mathcal{B}(a_{hk}, b_{hk})} . \quad (3)$$

154 Here,  $p(y)$  denotes the pdf of a continuous-valued random variable  $y$ . In Eq. (3),  $a_{hk} > 0$  and  $b_{hk} > 0$   
 155 are real-valued scalar parameters of the beta distribution that correspond to the scaled power in the  $h$ -th  
 156 ( $h \in [1, H]$ ) frequency band when the state  $k \in [1, K]$  is active. The normalization term  $\mathcal{B}(a_{hk}, b_{hk})$  denotes  
 157 the beta function,  $\mathcal{B}(a_{hk}, b_{hk}) = \Gamma(a_{hk})\Gamma(b_{hk})/\Gamma(a_{hk} + b_{hk})$ , where  $\Gamma(x) = \int_0^\infty t^{x-1}e^{-t}dt$  for any scalar  
 158 real-valued  $x > 0$ .

159 Our assumption of statistical independence across the  $H$  distinct frequency bands conditioned on an  
 160 underlying state, as implied in Eq. (3), leads to the conditional joint pdf (jpdf) on  $\mathbf{y}_n$ ,

$$161 \quad p(\mathbf{y}_n|z_n = k; \phi_k) = \prod_{h=1}^H p(y_{nh}|z_n = k; a_{hk}, b_{hk}) . \quad (4)$$

163 where  $\phi_k \equiv \{a_{hk}, b_{hk}\}_{h=1}^H$  corresponds to the set of  $2H$  beta distribution parameters associated with state  
 164  $k$ . The set of beta parameters across all states is denoted as  $\phi \equiv \{\phi_k\}_{k=1}^K$ . While the beta distribution  
 165 can be multimodal when both  $a_{hk}$  and  $b_{hk} \leq 1$ , we require that each state-specific pdf is unimodal. A  
 166 multimodal pdf associated with a latent state would indicate that the same state is associated with two  
 167 different spectral profiles, which will confound our intended interpretation of the states. Therefore, to ensure  
 168 the unimodality in the marginal pdf's we restrict the domain of the beta distribution parameters to avoid  
 169 scenarios when both  $a_{hk} \leq 1$  and  $b_{hk} \leq 1$  for a given  $h$  and  $k$ . In summary, we chose to work with the beta  
 170 distribution because it is a continuous probability distribution defined on the interval  $[0, 1]$ . Furthermore, it  
 171 is part of the exponential family which leads to efficient maximum likelihood estimation (section 2.4). The  
 172 beta distribution is highly flexible as it allows for unimodal distributions where the modes can lie anywhere  
 173 in  $[0, 1]$ .

### 174 2.3 State transition model

175 We assume the transition dynamics of the discrete-valued latent state process,  $z_n$ , to be governed by first-  
 176 order Markov transitions characterized by a constant transition probability matrix,  $\mathbf{A} = \{A_{jk}\}_{j=1, k=1}^{j=K, k=K}$ ,  
 177 such that

$$178 \quad Pr(z_n = k|z_{n-1} = j) = A_{jk} , \text{ where } \sum_{k=1}^K A_{jk} = 1 . \quad (5)$$

180 Here,  $Pr(z)$  denotes the probability mass function of a discrete-valued random variable  $z$ . The initial state  
 181 probability at the first time-window is characterized by a vector  $\boldsymbol{\pi} = \{\pi_k\}_{k=1}^K$  such that

$$182 \quad Pr(z_1 = k) = \pi_k , \text{ where } \sum_{k=1}^K \pi_k = 1 . \quad (6)$$

184 Together, the observation model (Eq. (4)), state transition matrix (Eq. (5)), and initial state probabilities  
 185 (Eq. (6)) define our state-space model, which we refer to as the *beta-HMM*.

## 186 2.4 Estimation of states and model parameters

187 We seek to determine the model parameters of the beta-HMM from one or more single channel LFP or EEG  
 188 LFP recordings using the maximum likelihood approach via the well-established Expectation-Maximization  
 189 (EM) algorithm [31, 33, 55, 56]. For a given set of  $L$  separate recording sessions,  $\{\mathbf{Y}_1, \dots, \mathbf{Y}_L\}$ , where the  
 190  $l$ -th session is denoted by  $\mathbf{Y}_l = \{\mathbf{y}_{n,l}\}_{n=1}^{N_l}$ , we assume that data can be described by an HMM associated  
 191 with the parameter set,  $\Theta = \{\{\boldsymbol{\pi}_l\}_{l=1}^L, \mathbf{A}, \boldsymbol{\phi}\}$ . Thus, we assume that the transition matrix,  $\mathbf{A}$ , and the state-  
 192 specific beta distribution parameters,  $\boldsymbol{\phi} = \{\boldsymbol{\phi}_k\}_{k=1}^K$ , remain constant across all  $L$  sessions, but the initial  
 193 state probability  $\boldsymbol{\pi}_l$  can vary across the sessions. When  $L = 1$  the problem reduces to learning a beta-HMM  
 194 using data from a single recording session as demonstrated later in Sec.4.2 with an LFP recording session  
 195 from an NHP. In this work (as shown in Sec. 4.3) we also learn subject specific beta-HMMs for 2 NHPs using  
 196  $L = 4$  separate recording LFP sessions from one NHP, and  $L = 5$  from the other. As shown in Sec. 4.4 we  
 197 also learn a beta-HMM for a typical patient using  $L = 9$  independent EEG recording sessions each from a  
 198 separate human subject. For  $L \geq 1$  mutually independent recording sessions the complete data likelihood  
 199 for a given  $\Theta$  can be written as,

$$\begin{aligned}
 200 \quad p(\{\mathbf{Y}_1, \mathbf{Z}_1, \dots, \mathbf{Y}_L, \mathbf{Z}_L\}|\Theta) &= \prod_{l=1}^L p(\mathbf{Y}_l, \mathbf{Z}_l|\boldsymbol{\pi}_l, \mathbf{A}, \boldsymbol{\phi}) \\
 201 \quad &= \prod_{l=1}^L \left( Pr(z_{1,l}|\boldsymbol{\pi}_l) \prod_{n=2}^{N_l} Pr(z_{n,l}|z_{n-1,l}, \mathbf{A}) \prod_{n=1}^{N_l} p(\mathbf{y}_{n,l}|z_{n,l} = k; \boldsymbol{\phi}_k) \right) \\
 202 \quad &= \prod_{l=1}^L \left( \pi_{z_{1,l}} \prod_{n=2}^{N_l} A_{z_{n-1,l} z_{n,l}} \prod_{n=1}^{N_l} \prod_{h=1}^H p(y_{nh,l}|z_{n,l} = k; a_{hk}, b_{hk}) \right) \quad (7) \\
 203
 \end{aligned}$$

204 where subscript  $(\cdot)_l$  denotes the random processes corresponding to the data sequence  $\mathbf{Y}_l$ . In the above  
 205 expression,  $\mathbf{Z}_l \equiv \{z_{1,l}, \dots, z_{N_l,l}\}$  denotes the sequence of latent states corresponding to  $\mathbf{Y}_l$ . In the ensu-  
 206 ing discussion, we shall refer to the expression,  $\log(p(\{\mathbf{Y}_1, \mathbf{Z}_1, \dots, \mathbf{Y}_L, \mathbf{Z}_L\}|\Theta))$ , as the complete data log-  
 207 likelihood. Note that by marginalizing over all possible  $\{\mathbf{Z}_1, \dots, \mathbf{Z}_L\}$ , we are able to obtain the likelihood  
 208 of  $\{\mathbf{Y}_1, \dots, \mathbf{Y}_L\}$  given the model,  $p(\{\mathbf{Y}_1, \dots, \mathbf{Y}_L\}|\Theta)$ .

209 The structure of the likelihood expression (Eq. (7)) allows for the maximum likelihood beta-HMM to  
 210 be estimated in terms of the parameter set  $\Theta = \{\{\boldsymbol{\pi}_l\}_{l=1}^L, \mathbf{A}, \boldsymbol{\phi}\}$  using the EM algorithm [31, 33, 55, 56].  
 211 The EM algorithm is commonly used for HMMs (the case of  $L = 1$  being the most familiar case [33]) with  
 212 observation distributions from the exponential family (e.g. the Gaussian distribution) [31, 33, 57, 58]. Briefly,  
 213 the standard EM algorithm is an iterative optimization scheme where in each EM iteration, we perform an E-  
 214 step followed by an M-step. In the E-step, following [31, Eq. 13.17], we run  $L$  independent *Forward-Backward*  
 215 algorithms ([31, 33]) to estimate the sequences  $\{\boldsymbol{\gamma}_{n,l}\}_{n=1}^{N_l} \equiv \{Pr(z_{n,l} = k|\mathbf{Y}_l, \hat{\boldsymbol{\pi}}_l, \hat{\mathbf{A}}, \hat{\boldsymbol{\phi}})\}_{n=1}^{N_l}$  (i.e. the posterior  
 216 probability of each state at each time-point) and  $\{\boldsymbol{\xi}_{n,l}\}_{n=1}^{N_l} \equiv \{Pr(z_{n-1,l} = j, z_{n,l} = k|\mathbf{Y}_l, \hat{\boldsymbol{\pi}}_l, \hat{\mathbf{A}}, \hat{\boldsymbol{\phi}})\}_{n=1}^{N_l}$   
 217 (i.e. the posterior probability of each state transition) given the observations ( $\{\mathbf{Y}_1, \dots, \mathbf{Y}_L\}$ ) and the last  
 218 best estimate of the model parameters ( $\hat{\Theta} = \{\{\hat{\boldsymbol{\pi}}_l\}_{l=1}^L, \hat{\mathbf{A}}, \hat{\boldsymbol{\phi}}\}$ ) from the previous iteration. Note that the  
 219 likelihood value,  $p(\{\mathbf{Y}_1, \dots, \mathbf{Y}_L|\hat{\Theta}\})$ , can also be readily calculated following the forward-step of the Forward-  
 220 Backward algorithm [31, 33].

221 The M-step of each iteration of the EM algorithm is posed as a maximization (over the space of allowable  
 222 parameters  $\Theta$ ) of the *expectation* of the complete data log-likelihood function, denoted by  $Q(\Theta, \hat{\Theta})$  and

223 defined as,

$$\begin{aligned}
 224 \quad Q(\Theta, \hat{\Theta}) &= \mathbb{E}_{\{\mathbf{Z}_1, \dots, \mathbf{Z}_L\} | \{\mathbf{Y}_1, \dots, \mathbf{Y}_L\}, \hat{\Theta}} \left[ \log \left( \prod_{l=1}^L p(\mathbf{Y}_l, \mathbf{Z}_l | \Theta) \right) \right] \\
 225 \quad &= \sum_{\{\mathbf{Z}_1, \dots, \mathbf{Z}_L\}} Pr(\{\mathbf{Z}_1, \dots, \mathbf{Z}_L\} | \{\mathbf{Y}_1, \dots, \mathbf{Y}_L\}, \hat{\Theta}) \sum_{l=1}^L \log p(\mathbf{Y}_l, \mathbf{Z}_l | \Theta) \\
 226 \quad &= \sum_{l=1}^L \sum_{\mathbf{Z}_l} Pr(\mathbf{Z}_l | \mathbf{Y}_l, \hat{\Theta}) \log p(\mathbf{Y}_l, \mathbf{Z}_l | \Theta) \\
 227 \quad &= \sum_{l=1}^L \sum_{k=1}^K \gamma_{1,l}(k) \log \pi_{k,l} + \sum_{l=1}^L \sum_{n=2}^{N_l} \sum_{j=1}^K \sum_{k=1}^K \xi_{n,l}(j, k) \log A_{jk} \\
 228 \quad &+ \sum_{l=1}^L \sum_{n=1}^{N_l} \sum_{k=1}^K \gamma_{n,l}(k) \log \prod_{h=1}^H p(y_{nh,l} | z_{n,l} = k; a_{hk}, b_{hk}) \tag{8} \\
 229
 \end{aligned}$$

230 where the last equality follows from Eq. (7). The expectation operation (denoted by  $\mathbb{E}$ ) indicated in the  
 231 first equality of Eq. (8) is based on the joint posterior probability distribution on the latent state trajectory  
 232 estimated using the last best estimate ( $\hat{\Theta}$ ) of the HMM. In the M-step, we determine the values for  $\{\pi_l\}_{l=1}^L$ ,  
 233  $\mathbf{A}$  and  $\phi$  that maximize  $Q(\Theta, \hat{\Theta})$  in Eq. (8), which we then use to update  $\hat{\Theta}$ . Additional constraints on this  
 234 maximization problem are given by the equality constraints on  $\mathbf{A}$  (Eqs. (5)) and on  $\pi$  (Eq. (6)), and the  
 235 following inequality constraints:  $A_{jk} \geq 0$ ,  $\pi_k \geq 0$ ,  $a_{hk}^2 + b_{hk}^2 - 2 > 0$  for all  $j, k \in [1, K]$  and  $h \in [1, H]$ . The  
 236 last set of inequality constraints on the beta pdf parameters leads to unimodal beta pdf's.

237 For an exponential family of observation distributions, the sequence of  $\hat{\Theta}$ 's, resulting from maximizing  
 238  $Q(\Theta, \hat{\Theta})$  in each EM iteration, leads to a monotonic approach to a maxima of the likelihood function [59, 57,  
 239 58, 33]. Therefore, we use the estimated log-likelihood to track EM-algorithm convergence, i.e. we terminate  
 240 the EM algorithm at an iteration number,  $t$ , when  $p(\{\mathbf{Y}_1, \dots, \mathbf{Y}_L\} | \hat{\Theta}^{(t)}) - p(\{\mathbf{Y}_1, \dots, \mathbf{Y}_L\} | \hat{\Theta}^{(t-1)}) < 0.0001$ .  
 241 Since the EM algorithm is known to converge to a local maxima [59], we repeat the EM algorithm with  
 242 multiple initial guesses of  $\Theta$  and choose the set of model parameters with the highest likelihood. Essential  
 243 steps relevant to the M-step are presented in the appendix (Sec. A).

244 Furthermore, using the ML beta-HMM we solve for the optimal state trajectory  $\{z_{n,l}^*\}_{n=1}^{N_l} = \arg \max_{\mathbf{Z}_l}$   
 245  $p(\mathbf{Y}_l, \mathbf{Z}_l | \hat{\Theta})$  using the *Viterbi* algorithm [31, Sec. 13.2]. This state trajectory represents the unsupervised  
 246 segmentation of the data sequence,  $\mathbf{Y}_l$ . The output of the HMM fitted to the multiple observations from  
 247 multiple sessions are the estimates of the ML parameter set,  $\hat{\Theta}$ , and corresponding sequences of  $\{\{\gamma_{n,l},$   
 248  $\xi_{n,l}, z_{n,l}^*\}_{n=1}^{N_l}\}_{l=1}^L$ . Since the assignment of state label is random, we re-number the states from 1 to  $K$  in  
 249 the ascending order of the mean ( $= a_{Hk}/(a_{Hk} + b_{Hk})$ ) of the beta distributions corresponding to the  $H$ -th  
 250 frequency band.

## 251 2.5 Statistical analysis using beta-HMM parameters

252 The estimated beta-HMM provides reduced-order summaries of the scaled spectral dynamics. Between any  
 253 two states, we can compare the spectral power in a given frequency band, as well as duration statistics  
 254 derived from the transition matrix.

255 **Summarizing scaled spectral power in a given frequency band:** The set of beta distributions  
 256 provides rich information about the scaled spectral observations. One helpful statistic to summarize each

257 beta distribution is  $Pr(Y_h > 0.5|Z = k)$  where  $(Y_h|Z = k) \sim Beta(a_{hk}, b_{hk})$  (see glossary in Table 1). For  
 258 example, when this probability is high, we can say that the scaled power for the  $k$ -th state and  $h$ -th frequency  
 259 band is primarily distributed between  $[0.5, 1]$ . According to Eq. (2), this also indicates high spectral power  
 260 in the  $h$ -th frequency band for the time-points when the state  $k$  is active.

261 **Comparing scaled spectral power in a given frequency band between any two beta-HMM**  
 262 **states:** One way to quantify how different any pair of beta distributions are from one another is to calculate  
 263 the Kolmogorov-Smirnoff (KS)-distance from a large number of samples generated from the two distributions  
 264 (we use 100,000 samples here). The KS-distance measures the maximum difference between two empirical  
 265 CDFs, so values close to zero indicate that the underlying distributions are similar, and larger values indicate  
 266 that the underlying distributions are dissimilar. Alternatively, we can leverage the analytic tractability of the  
 267 beta distributions to analyze a difference random variable,  $\Delta_{hjk} = X_{hj} - X_{hk}$ , where  $X_{hj} \sim Beta(a_{hj}, b_{hj})$   
 268 and  $X_{hk} \sim Beta(a_{hk}, b_{hk})$ . Here, the parameter sets  $\{a_{hj}, b_{hj}\}$  and  $\{a_{hk}, b_{hk}\}$  respectively correspond to a  
 269 state  $j$  and another state  $k$  in the  $h$ -th frequency band. We use  $Pr(\Delta_{hjk} \leq 0)$  to denote the cumulative  
 270 distribution function (cdf) value at 0 for  $\Delta_{hjk} \in [-1, 1]$  such that

$$271 \quad Pr(\Delta_{hjk} \leq 0; a_{hj}, b_{hj}, a_{hk}, b_{hk}) = \int_{-1}^0 p(\delta; a_{hj}, b_{hj}, a_{hk}, b_{hk}) d\delta \quad (9)$$

273 where, the pdf of the random variable  $\Delta_{hjk}$  can be expressed at a given realization  $\delta$  as,

$$274 \quad p(\delta; a_{hj}, b_{hj}, a_{hk}, b_{hk}) = \begin{cases} \int_0^{1+\delta} p(x_{hj}, \delta) dx_{hj} & -1 < \delta \leq 0 \\ \int_{\delta}^1 p(x_{hj}, \delta) dx_{hj} & 0 < \delta < 1 \end{cases} \quad (10)$$

276 where the joint pdf  $p(x_{hj}, \delta)$  is defined as,

$$277 \quad p(x_{hj}, \delta) = \frac{x_{hj}^{a_{hj}-1} (1-x_{hj})^{b_{hj}-1}}{B(a_{hj}, b_{hj})} \times \frac{(x_{hj}-\delta)^{a_{hk}-1} (1-x_{hj}+\delta)^{b_{hk}-1}}{B(a_{hk}, b_{hk})}. \quad (11)$$

279 For example, if  $Pr(\Delta_{hjk} \leq 0) = \alpha$ , then there is probability of  $\alpha$  that  $X_{hj} \leq X_{hk}$ , or equivalently a  
 280 probability of  $1-\alpha$  that  $X_{hj} > X_{hk}$ <sup>2</sup>. In the ensuing discussion we adopt the following notational convention  
 281 for clarity. For a within-subject pairwise comparison of HMM states estimated for a single NHP (see section  
 282 4.3), we add a superscript indicating the NHP (e.g.  $\Delta_{hjk}^{MJ} = X_{hj}^{MJ} - X_{hk}^{MJ}$ , for NHP MJ). When we compare  
 283 states between two NHPs, we add superscripts indicating both NHPs (e.g.  $\Delta_{hjk}^{MJ,LM} = X_{hj}^{MJ} - X_{hk}^{LM}$ , when  
 284 comparing an HMM state from NHP MJ to one from NHP LM). When we perform pairwise comparison of  
 285 HMM states estimated from the human OR dataset (see section 4.4), we add the superscript H,  $\Delta_{hjk}^H$ .

286 **Comparing duration statistics between (i) any two beta-HMM states, and (ii) any two**  
 287 **neurophysiological states each characterized by one or more beta-HMM states:** We present  
 288 several statistics to describe the dynamics of the model. If  $d_k$  indicates a positive integer-valued random  
 289 variable of the duration spent in state  $k$  after transitioning into it and before transitioning out to a different

<sup>2</sup>A general approach to calculate probability distributions for difference random variables can be found in the work by Cook and Nadarajah[60]

290 state, then the *mean duration* in that HMM state is given by

$$291 \quad \hat{d}_k = \sum_{d=1}^{\infty} d_k Pr(d_k) = \frac{1}{1 - A_{kk}} \quad (12)$$

292

293 where  $Pr(d_k) \equiv Pr(z_{n:n+d_k} = k | z_n = k, z_{n-1} \neq k) = (1 - A_{kk})A_{kk}^{d_k-1}$ , which holds for any  $n > 1$  [33]. Here,  
294 the subscript  $(\cdot)_{,l}$  denoting the data sequence is omitted for brevity.

295 In cases where a subset of beta-HMM states,  $\mathbf{k}^* \subset \{1, \dots, K\}$  corresponds to a neurophysiological  
296 phenomenon of interest (e.g. multiple HMM states corresponding to sub-states of gamma burst activity,  
297 or, multiple HMM states corresponding to the period between two consecutive gamma bursts), we use the  
298 following Monte Carlo approach to estimate the consecutive time spent in this subset of beta-HMM states.  
299 Using the estimated transition matrix  $\hat{\mathbf{A}}$  and randomly sampled state  $z_1$ , we generate a Markov sequence,  
300  $z_{1:N}$  ( $N = 2000$  in our study). For all  $z_n$ 's taking values in  $\mathbf{k}^*$ , the corresponding state label is reassigned  
301 as  $z_n = 1$ . The states that do not take values in  $\mathbf{k}^*$  are reassigned values as  $z_n = 0$ . We then calculate the  
302 mean duration spent in the neurophysiological state,  $\hat{d}_{k^*}$ , as the mean number of consecutive time points  
303 where  $z_n = 1$  holds. Similarly, for the same neurophysiological state  $\mathbf{k}^*$  we also calculate a *mean interval*  
304 statistic as the average number of consecutive timepoints where  $z_n = 0$ ; this is an estimate of the time  
305 interval between the two consecutive occurrences of  $\mathbf{k}^*$ . By repeating this procedure  $N_{MC}$  times ( $= 4000$  in  
306 our study) we calculate median and 95% confidence intervals of the state-specific mean duration and mean  
307 interval statistics, together referred to as the duration statistics in the ensuing discussion.

### 308 **3 Experimental Recordings**

#### 309 **3.1 NHP LFP recordings under ketamine anesthesia**

310 All NHP procedures reported here followed the guidelines of the Massachusetts Institute of Technology's  
311 Committee on Animal Care and of the National Institutes of Health. LFPs were recorded in multiple  
312 separate recording sessions from two rhesus macaques (*Macaca mulatta*) aged 14 years (NHP MJ, male, 13.0  
313 kg) and 8 years (NHP LM, female, 6.6 kg). LFP recordings from 4 sessions in NHP MJ and 5 sessions in  
314 NHP LM were analyzed in this study. During each recording session, ketamine was administered as a single  
315 20 mg/kg bolus intramuscular dose. This is a putative high dose for sedation and low dose for surgical  
316 anesthesia in NHPs [61, 62, 63]. Fifteen minutes prior to ketamine administration, glycopyrrolate (0.01  
317 mg/kg) was delivered to reduce salivation and airway secretions. In both NHPs, LFPs were recorded from  
318 a  $8 \times 8$  iridium-oxide contact microelectrode array ("Utah array", MultiPort: 1.0 mm shank length, 400  
319  $\mu\text{m}$  spacing, Blackrock Microsystems, Salt Lake City, UT) implanted in the prefrontal cortex (area 8A).  
320 LFPs, recorded at 30 kHz, were low-pass filtered to 250 Hz and then downsampled to 1 kHz. LFPs were  
321 continuously recorded from 1–5 minutes prior to ketamine injection up to 18–20 minutes following ketamine  
322 injection. In the ensuing figures representing neural timeseries data, the time 0 denotes the time-point when  
323 the ketamine bolus was administered.

#### 324 **3.2 Human EEG recordings under ketamine anesthesia**

325 The Partners Institutional Review Board approved this human retrospective observational study. The data  
326 analyzed in this manuscript were acquired during an EEG study of ketamine-induced general anesthesia. We

327 reviewed and selected 9 patients (Age:  $51.8 \pm 11.7$  years, Weight:  $84.5 \pm 15.5$  kg, mean  $\pm$  standard deviation)  
328 from our database who were administered an intravenous bolus dose of ketamine as the sole hypnotic drug  
329 for the induction of general anesthesia. The ASA scores in all these 9 patients were less than or equal to 3,  
330 and none of the patients had a history of any neurological or psychiatric disorders. Prior to the ketamine  
331 bolus, patients were administered midazolam (n=8;  $1.81 \pm 0.53$  mg) and/or fentanyl (n=7;  $164.29 \pm 80.18$   
332 mcg) for anxiolysis and to block the sympathetic response to laryngoscopy, respectively. To induce general  
333 anesthesia (GA) a bolus dose of ketamine (mean  $\pm$  standard deviation;  $182.22 \pm 29.06$  mg, 10 mg/ml)  
334 was administered, and intubation was carried out using succinylcholine, cisatracurium, or rocuronium for  
335 muscle relaxation. EEG data were acquired using Sedline monitor (Masimo Inc, USA). The standard Sedline  
336 Sedtrace electrode arrays were placed on the forehead that approximated the positions of Fp1, Fp2, F7, and  
337 F8, the ground electrode at Fpz, and the reference electrode 1 cm above Fpz. For our analysis, we use the  
338 data recorded from Fp2. Data were recorded with a pre-amplifier bandwidth of 0.5 to 92 Hz, a sampling  
339 rate of 250 Hz, with 16-bit, 29 nV resolution. Electrode impedance was less than 5 k $\Omega$  in each channel. We  
340 analyzed continuous EEG recordings starting from 2 minutes pre-ketamine bolus and up to 5.5 min - 14 min  
341 post-ketamine bolus, and prior to the administration of any additional hypnotic drugs used to maintain GA.

## 342 4 Results

### 343 4.1 Testing the beta-HMM analysis framework against simulated ground truth

344 To test the ability of our beta-HMM analysis framework to accurately retrieve a known Markov sequence and  
345 associated observation distributions, we simulated spectrograms generated by pre-specified Markov processes  
346 (See Table 2 in the appendix for simulation algorithm). We simulated spectral dynamics comparable to those  
347 caused by ketamine by using a spectrogram  $S_n(\cdot)$  calculated from one session of NHP experimental data (as  
348 described in Sec 2.1) as input to the algorithm (Table 2 in the appendix). Additional inputs to this algorithm  
349 are user-prescribed HMM parameters, the number of states  $K$ ,  $\boldsymbol{\pi}$  and  $\mathbf{A}$ , as well as the duration  $M$  of the  
350 simulated data. This algorithm outputs a realization of the latent state path,  $\mathbf{z} = \{z_m\}_{m=1}^M$ , corresponding  
351 simulated spectrogram,  $S_m^{sim}(\boldsymbol{\omega})$ , and  $\mathbf{Y}$ . While  $S_m^{sim}(\boldsymbol{\omega})$  is used for visualization, the realization of  $\mathbf{Y}$   
352 serves as the observations from which we estimate a  $K$ -state beta-HMM (Sec. 2.4). Salient features of the  
353 algorithm in Table 2 of the appendix are as follows. First,  $K$  distinct spectral clusters are created from the  
354 given NHP LFP spectrogram using an unsupervised clustering algorithm (different from beta-HMM) that  
355 does not respect the dependence across consecutive time-points. Then a Markov sequence is simulated using  
356 the known parameters,  $\boldsymbol{\pi}$  and  $\mathbf{A}$ . Finally, to generate the spectrogram with  $K$  underlying latent states with  
357 Markov state transitions, a spectrum is selected for a given instant by uniformly sampling from one of the  
358  $K$  spectral clusters that corresponds to the realization of the latent state at the same instant.

359 For a given  $K$ , we generate 100 realizations of  $\mathbf{Y}$  based on  $K$  spectral clusters. For each realization of  
360  $\mathbf{Y}$ , we estimate a  $K$ -state beta HMM to determine a set of estimated model parameters  $\hat{\Theta} = \{\hat{\boldsymbol{\pi}}, \hat{\mathbf{A}}, \hat{\boldsymbol{\phi}}\}$ ,  
361 and the estimated state path  $\mathbf{z}^*$  (calculated using the Viterbi algorithm). We assess goodness of fit for each  
362 realization of  $\mathbf{Y}$  by comparing the estimated state path,  $\mathbf{z}^*$ , and model parameters,  $\hat{\Theta}$ , to the ground truth  
363 state path,  $\mathbf{z}$ , and model parameters,  $\Theta$ , respectively.

364 To assess the accuracy of the estimated path  $\mathbf{z}^*$  compared to the known path  $\mathbf{z}$ , we calculated the fraction

365 of time points for which the estimated and known path are identical:

$$366 \quad \text{Path Accuracy} = \frac{\sum_{n=1}^N I(z_n, z_n^*)}{N}, \text{ where } I(z_n, z_n^*) = \begin{cases} 0 & z_n \neq z_n^* \\ 1 & z_n = z_n^* \end{cases} \quad (13)$$

367

368 To assess the accuracy of the observation distribution estimation, we calculated the mean KS-distance  
 369 between the *HK* ground truth and estimated beta distributions. KS-distances close to zero indicate that the  
 370 estimated and ground truth distributions are similar. We also calculated the absolute errors in the estimated  
 371 initial state and state transition probabilities, denoted respectively by  $\epsilon_A$  and  $\epsilon_\pi$ ,

$$372 \quad \epsilon_A = \frac{\sum_{j=1}^K \sum_{k=1}^K |A_{jk} - \hat{A}_{jk}|}{2K} \quad (14)$$

$$373 \quad \epsilon_\pi = \frac{\sum_{k=1}^K |\pi_k - \hat{\pi}_k|}{2} \quad (15)$$

374

375 Note the the maximum possible value for  $\sum_{j=1}^K \sum_{k=1}^K |A_{jk} - \hat{A}_{jk}| = 2K$  and for  $\sum_{k=1}^K |\pi_k - \hat{\pi}_k| = 2$ . Thus,  
 376 the denominators scale the absolute errors to the range of  $[0, 1]$ . We report the median and 90% confidence  
 377 intervals of each of these metrics calculated across 100 simulated spectrograms for each model order in Fig. 2.

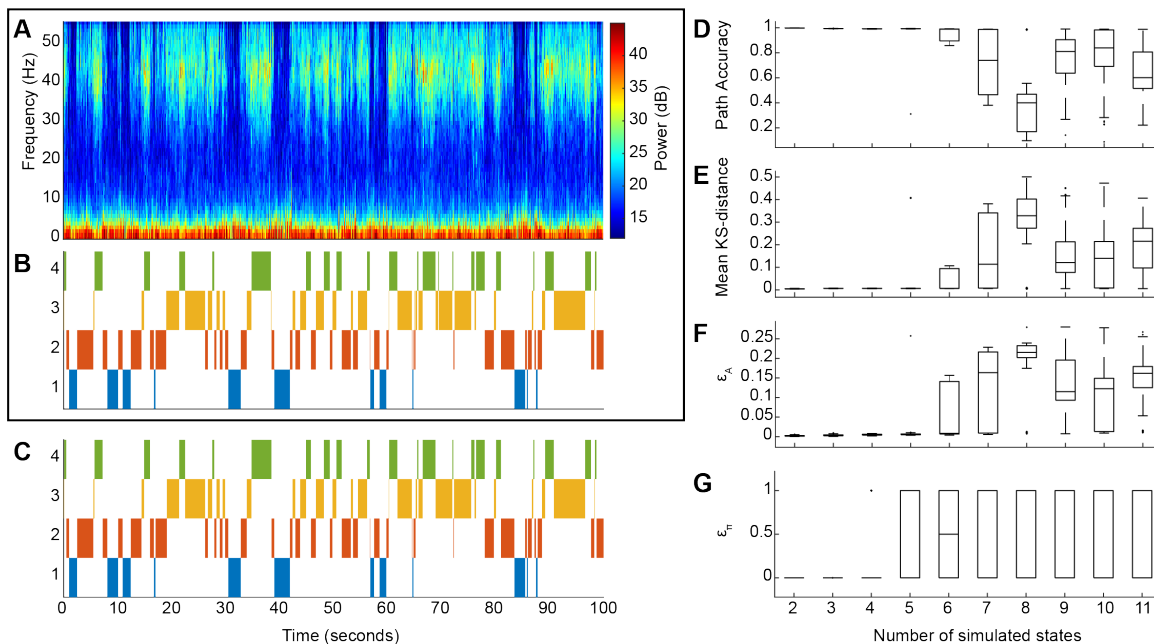


Figure 2: **The beta-HMM tracks the dynamic structure of simulated spectrograms characterized by discrete state transitions** (extracted from one sequence of ketamine-induced LFP in NHP MJ). (A) One realization of simulated spectrogram. (B) Markov path corresponding to the simulated spectrogram in panel A. (C) Optimal state trajectory estimated from simulated data in panel A via the beta-HMM analysis. (D-G) Goodness of fit analysis. Box-plots summarize the state path accuracy (Eq. (13)) in panel D, the KS-distance between the estimated and the actual state-specific and frequency band-specific beta distributions (averaged across all states and all frequency bands) in panel E, the relative error in transition matrix (Eq. (14)) in panel F, and relative error in the initial state probabilities (Eq. (15)) in panel G. For each specified number of states, 100 realizations of spectrograms were simulated and the beta-HMM analysis was performed on each.

378 Simulation analysis revealed that the model parameters of simulated spectrograms, generated from  
379 ketamine-induced neural data and characterized by known Markov transition dynamics, can be accurately  
380 estimated with the beta-HMM framework for low model orders. The performance of the beta-HMM analysis  
381 framework on a typical simulated spectrogram (Fig. 2(A)) demonstrates that the estimated state trajectory  
382 (Fig. 2(C)) matches well with the actual state trajectory (Fig. 2(B)). Across 400 simulated datasets for  
383 models with 2 through 5 states (100 simulations each), the estimated state trajectory was estimated with  
384 high accuracy (*Path Accuracy* > 0.98 for all but one of 400 independent simulations), the beta distributions  
385 were estimated with high accuracy (mean KS-distance <  $7.76 \times 10^{-3}$  for all but one of 400 independent  
386 simulations) and the transition matrix was estimated with low relative error ( $\epsilon_A < 0.01$  for all but one of  
387 400 independent simulations). For models with 2-3 states, the initial probability, which corresponds to a  
388 single data point, was also accurately estimated ( $\epsilon_\pi < 2.45 \times 10^{-14}$ ). Beyond 5 states, there was a significant  
389 drop-off in estimation accuracy. A potential reason for this occurrence is redundancy across some of the  
390  $K > 5$  spectral clusters derived from the original NHP spectrogram, which may not contain more than 5  
391 clusters of distinct neural activity. Overall, this numerical experiment generated detailed insights on the  
392 level of inaccuracy in our beta-HMMs when estimated from spectral data derived from real neural activity  
393 induced by ketamine.

## 394 4.2 Demonstration of the beta-HMM analysis on a single observation sequence 395 of NHP LFP data ( $L = 1$ case)

396 Using the numerically tested beta-HMM analysis framework, we analyzed a single session high-dose ketamine  
397 NHP LFP recording (Sec 3). From qualitative analysis of the time-series data and as well as spectral estimates  
398 (Fig. 9 in Supporting Figures section), we identified 4 key signatures induced by ketamine: a *slow oscillation*  
399 *state* with a prominent low-frequency (0-10 Hz) activity and negligible activity in the gamma band (30-50  
400 Hz); a transition state with simultaneous activity in 0-10 Hz and 30-50 Hz bands; and two others with  
401 significant but differing levels of gamma activity and relatively lower low-frequency activity, which we refer  
402 to as *gamma burst states*. We also sought to capture the transition from pre- to post- ketamine bolus  
403 neurophysiology, so we chose a model order of  $K = 5$ . We estimated a 5-state beta-HMM from a single  
404 sequence of LFP spectrogram.

405 The 5-state beta-HMM provided a quantitative characterization of the neurophysiological dynamics in-  
406 duced by ketamine (see Fig. 3(A, B), as well as Fig. 10 in the Supporting Figures section). The beta-HMM  
407 analysis objectively identified gamma-slow dynamics in NHPs similar to those described by [11]. We found  
408 that the HMM identified alternating states which corresponded to periods of prominent gamma oscillations,  
409 prominent slow oscillations in the absence of gamma, and an intermediate state in between (Fig. 3(C, D)).  
410 From visual inspection of the the state-segmented spectrograms and further analysis of beta distributions  
411 (Fig. 3(E, F)), we identified the relevant neurophysiological states with distinct spectral signatures. For  
412 example, in the state-segmented spectrogram for state 5 (Figure 3E), we can see that high spectral power  
413 in the 30-40 Hz frequency band ( $h = 4$ ) is associated with a high probability that  $(Y_4|Z = 5) > 0.5$  (Fig-  
414 ure 3F)<sup>3</sup>. Based on the beta distributions, we found that HMM states 4 and 5 both have high gamma  
415 power (30-40 Hz ( $h = 4$ ):  $Pr(Y_4 > 0.5|Z = 4) = 0.98$ ,  $Pr(Y_4 > 0.5|Z = 5) = 1.00$ ; 40-50 Hz ( $h = 5$ ):  
416  $Pr(Y_5 > 0.5|Z = 4) = 0.98$ ,  $Pr(Y_5 > 0.5|Z = 5) = 0.97$ ). HMM state 2 is dominated by prominent slow

<sup>3</sup>See Sec B for a tutorial-styled explanation of how the estimated beta pdf's are used to analyze the spectral properties of the HMM states

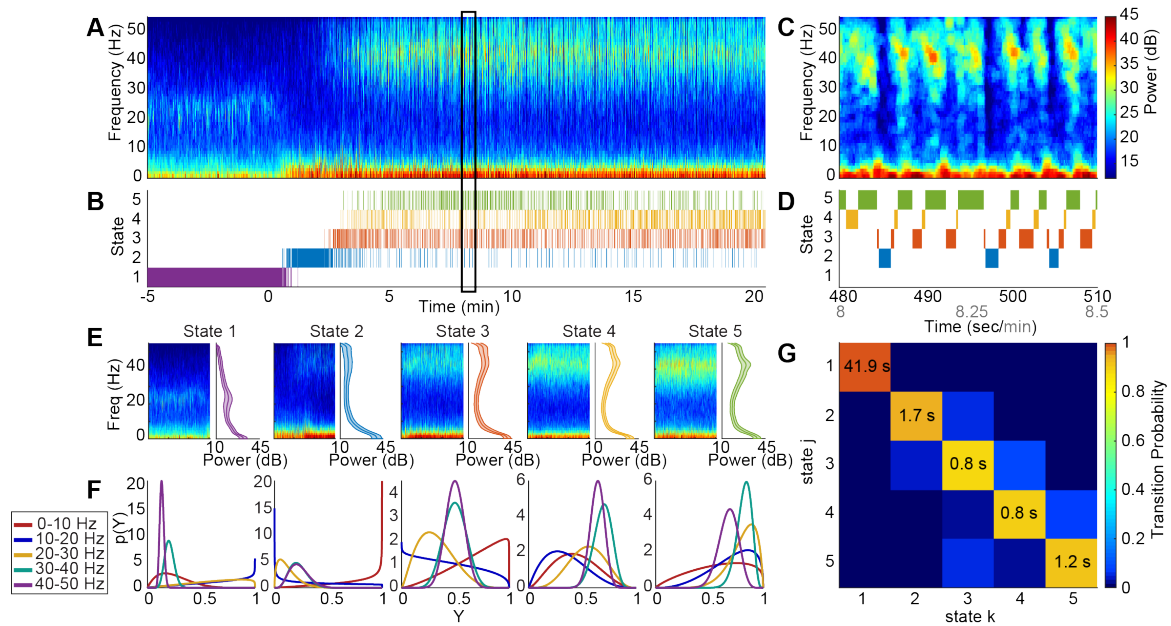


Figure 3: **A 5-state beta-HMM estimates ketamine-induced neurophysiological dynamics from a single NHP LFP sequence.** (A) Multitaper spectrogram of LFP where time 0 marks the time-point of administration of 20 mg/kg ketamine intramuscular bolus. (B) Estimated latent state trajectory. (C) Enlarged view of panel A for the epoch identified by the rectangular box. (D) Enlarged view of panel B for the epoch identified by the rectangular box. (E) Spectral clusters identified by the 5-state beta-HMM. Each spectral cluster has a characteristic signature as indicated by the mean spectrum and corresponding standard deviation. (F) Frequency-band specific beta distributions (over scaled power (Y) in respective bands) estimated for each of the 5 states. (G) The estimated transition matrix. The expected value of the duration spent in each state is indicated on the diagonal.

417 power (0-10 Hz ( $h = 1$ ):  $Pr(Y_1 > 0.5|Z = 2) = 0.82$ ) and low gamma power ( $Pr(Y_4 > 0.5|Z = 2) = 0.00$ ,  
418  $Pr(Y_5 > 0.5|Z = 2) = 0.00$ ). Therefore, we consider HMM states 4 and 5 together to represent the neuro-  
419 physiological gamma burst state, HMM state 2 to represent the slow oscillation state, and HMM state 3 to  
420 represent the transition between neurophysiological slow oscillation and gamma burst states.

421 The transition matrix (Fig. 3G) quantifies the alternating dynamics noted in Fig. 3(C, D). From the  
422 transition matrix, we can also determine the expected duration of each state, as denoted on the diagonal  
423 terms indicating self-transition probabilities (Eq. 12). From the transition probabilities and optimal state  
424 trajectory, we infer there is a high probability of the state sequence  $2 \rightarrow 3 \rightarrow 4 \rightarrow 5 \rightarrow 3 \rightarrow 2$ . This confirms  
425 the alternating dynamics between time-localized high power activity in the gamma and low frequency bands  
426 induced by ketamine. The beta-HMM provides further evidence that the neural activity induced by ketamine  
427 is distinct from pre-ketamine neural activity. States 2 through 5 do not occur prior to the ketamine bolus  
428 (Fig. 3(A, B)). Furthermore, HMM state 1 has sustained prevalence prior to the bolus and does not occur  
429 after a brief initial period (approximately 1 minute) post-bolus. Therefore, HMM state 1 can be associated  
430 with a pre-ketamine neurophysiological state. This is further supported by the fact that the transition  
431 probability from any of the post-bolus states back to state 1 is less than 0.003.

### 432 4.3 Subject-specific beta-HMMs estimated from multiple recording sessions 433 ( $L > 1$ case) from 2 NHPs

434 A review of summary statistics from session-specific beta-HMMs estimated from multiple recording sessions  
435 of each NHP indicated the presence of subject-specific HMM states that have common features (both spectral  
436 and temporal) across sessions. This further suggested the utility of a subject-specific HMM for each NHP.  
437 Therefore, we fitted two 5-state beta-HMMs to multiple LFP recording sessions from 2 NHPs: 4 sessions  
438 for NHP MJ and 5 sessions for NHP LM. A key implementation feature in our beta HMM analysis from  
439 multiple sessions (for a given group) is that we do not concatenate multiple sessions; rather we treat them as  
440 mutually independent in our EM algorithm implementation (as discussed in Sec. 2.4). Thus, the beta-HMM  
441 analysis respects the sequential nature of the observations within a session, while maintaining the distinction  
442 across multiple sessions. Since there were at least three days between each NHP session, we treated them  
443 as mutually independent and therefore utilized the EM algorithm based on Eq. (8) to estimate the model  
444 parameters.

445 We present the optimal state trajectories and state-specific and frequency band-specific observation dis-  
446 tributions estimated from all 9 sessions of 2 NHPs in Fig. 4 (also see Figs. 11 and 12 in the Supporting  
447 Figures section). Although the amplitude of the spectral power tended to vary across sessions, our use of  
448 scaled power facilitated identification of common states with similar spectral profiles across multiple sessions.  
449 In both NHPs, we found that the beta distributions in each frequency band were unique across all states (KS-  
450 distance  $> 0.05$  for all pairwise comparisons; 100 comparisons = 10 pairs of states per frequency band per  
451 NHP  $\times$  5 frequency bands  $\times$  2 NHPs) (Fig. 4(E,L)). Consistent with the single session observations in NHP  
452 MJ, in both primates we found that HMM state 5 has high scaled power in the 30-40 Hz range, and both  
453 HMM states 4 and 5 have high power in the 40-50 Hz range (NHP MJ:  $Pr(Y_4 > 0.5|Z = 5) = 1.00$ ,  
454  $Pr(Y_5 > 0.5|Z = 4) = 0.97$ ,  $Pr(Y_5 > 0.5|Z = 5) = 0.99$ ; NHP LM:  $Pr(Y_4 > 0.5|Z = 5) = 0.90$ ,  
455  $Pr(Y_5 > 0.5|Z = 4) = 0.71$ ,  $Pr(Y_5 > 0.5|Z = 5) = 0.97$ )<sup>4</sup>. We found that state 4 in NHP LM had  
456 comparatively lower scaled power in the 30-40 Hz range (NHP MJ:  $Pr(Y_4 > 0.5|Z = 4) = 0.95$ ; NHP LM:

<sup>4</sup>See Sec B for a tutorial-styled explanation of how the estimated beta pdf's are used to analyze the spectral properties of the HMM states

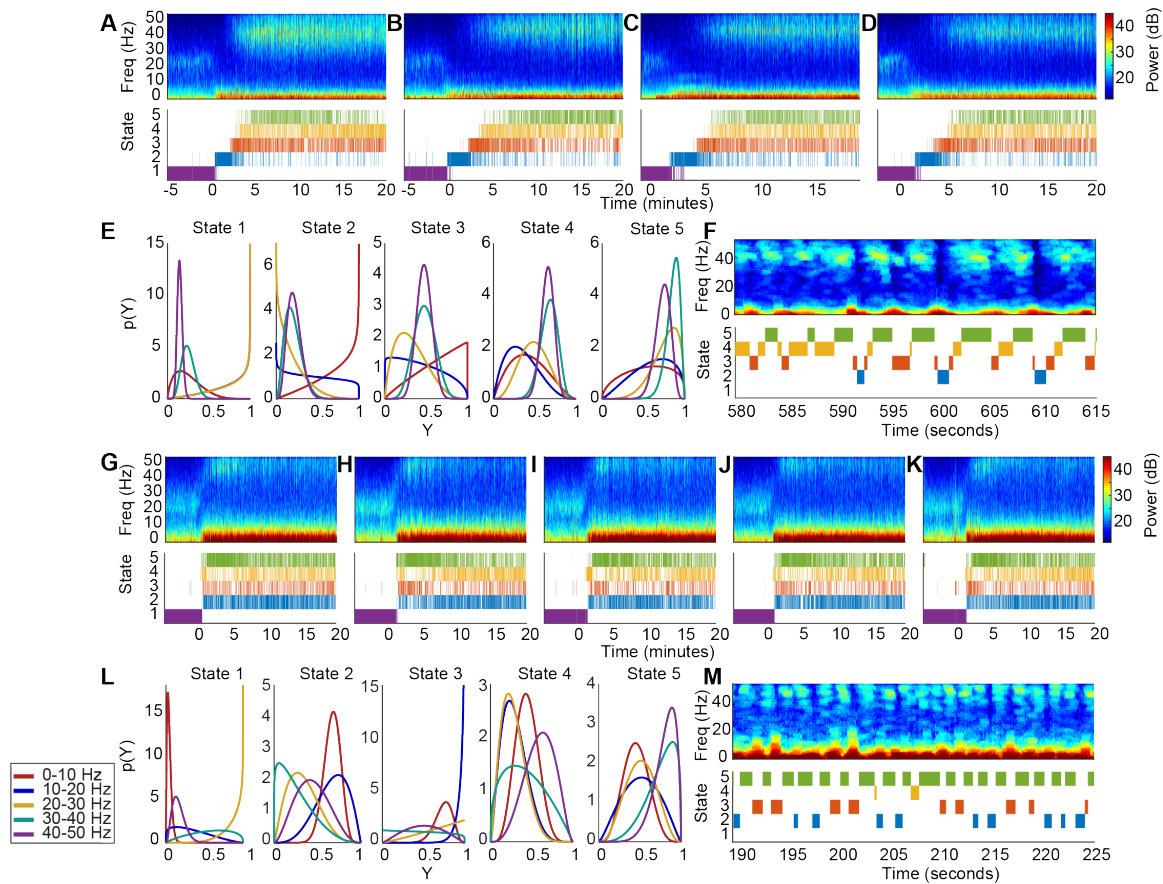


Figure 4: **The 5-state beta-HMM can be fit across multiple sessions to create an NHP-specific model.** (A-D) Multitaper spectrograms of LFP and corresponding estimated latent state trajectories from 4 sessions in NHP MJ. (E) Frequency band-specific beta pdfs for each of the 5 states estimated from the 4 sessions in NHP MJ (Y - scaled power) (F) Enlarged view of a typical 35s epoch in panel D. (G-K) Multitaper spectrograms of LFP and corresponding estimated latent state trajectories from 5 sessions in NHP LM. (L) Frequency band-specific beta pdfs for each of the 5 states estimated from the 5 sessions in NHP LM. (Y - scaled power) (M) Enlarged view of a typical 35s epoch in panel K.

457  $Pr(Y_4 > 0.5|Z = 4) = 0.36$ ). We also found in both NHPs that state 2 is dominated by prominent slow  
 458 power (NHP MJ:  $Pr(Y_1 > 0.5|Z = 2) = 0.81$ ; NHP LM:  $Pr(Y_1 > 0.5|Z = 2) = 0.96$ ) and low gamma power  
 459 (NHP MJ:  $Pr(Y_4 > 0.5|Z = 2) = 0.01$ ,  $Pr(Y_5 > 0.5|Z = 2) = 0.00$ ; NHP LM:  $Pr(Y_4 > 0.5|Z = 2) = 0.12$ ,  
 460  $Pr(Y_5 > 0.5|Z = 2) = 0.37$ ). Again, we consider HMM states 4 and 5 together to represent the neurophys-  
 461 iological gamma burst state, and HMM state 2 to represent the slow oscillation state. As demonstrated in  
 462 Fig. 3(C,D), the multisession beta-HMM model captures the alternating dynamics induced by ketamine in  
 463 both primates (Fig. 4(F,M)).

464 We use the subject-specific HMMs to further analyze the spectral content and duration statistics across  
 465 states, both within a subject as well as between the two subjects. We use the ML estimated beta distributions  
 466 to perform pairwise comparisons of the scaled power between any two states from either NHP (Fig. 5(A-D)).  
 467 By investigating  $Pr(\Delta_{hjk} \leq 0; a_{hj}, b_{hj}, a_{hk}, b_{hk})$  (per Sec. 2.5), we were able to determine the probability  
 468 that HMM state  $j$  had lower scaled power than HMM state  $k$  in the  $h$ -th frequency band. For this section,  
 469 we simplify the notation by referring to  $Pr(\Delta_{hjk} \leq 0; a_{hj}, b_{hj}, a_{hk}, b_{hk})$  as  $Pr(\Delta_{hjk} \leq 0)$ , and summarize the  
 470 key findings<sup>5</sup>. In both NHPs, we found that the scaled powers in the 0 – 10 Hz and 40 – 50 Hz bands during  
 471 the pre-ketamine state (HMM state 1) were lower relative to every other state ( $0.00 < Pr(\Delta_{hj,1}^{MJ} \leq 0) < 0.26$   
 472 and  $0.00 < Pr(\Delta_{hj,1}^{LM} \leq 0) < 0.09$  for  $h \in \{1, 5\}$  and  $j \in [2, K]$ ). This provides further evidence that  
 473 the oscillatory dynamics in these two frequency bands were most significantly altered by ketamine. NHP  
 474 MJ had higher scaled power in the 30-40 and 40-50 Hz ranges in states 4 and 5 compared to states 2 and  
 475 3 ( $0.00 < Pr(\Delta_{h,j,k}^{MJ} \leq 0) < 0.12$  for  $h \in [4, 5]$ ,  $j \in [4, 5]$ , and  $k \in [2, 3]$ ). This is consistent with the  
 476 observation that the gamma bursts (represented by states 4 and 5) in NHP MJ occurred broadly between  
 477 30-50 Hz. NHP LM also had higher scaled power in the 40-50 Hz range in states 4 and 5 compared to  
 478 states 2 and 3 ( $0.04 < Pr(\Delta_{5,j,k}^{LM} \leq 0) < 0.37$  for  $j \in [4, 5]$ , and  $k \in [2, 3]$ ). However, state 4 in NHP  
 479 LM did not have higher 30-40 Hz scaled power than state 3 ( $Pr(\Delta_{4,4,3}^{LM} \leq 0) = 0.55$ ). This is consistent  
 480 with the observation that the gamma bursts (represented by states 4 and 5) occurred primarily between  
 481 40-50 Hz in NHP LM. In both NHPs, state 2 had higher scaled power in the 0-10 Hz range compared to  
 482 states 4 and 5 ( $0.69 < Pr(\Delta_{1,j,2}^{MJ} \leq 0) < 0.83$  and  $0.88 < Pr(\Delta_{1,j,2}^{LM} \leq 0) < 0.92$  for  $j \in [4, 5]$ ), and lower  
 483 power in the 30-40 and 40-50 Hz ranges compared to states 3 to 5 ( $0.00 < Pr(\Delta_{h,j,2}^{MJ} \leq 0) < 0.03$  and  
 484  $0.05 < Pr(\Delta_{h,j,2}^{LM} \leq 0) < 0.41$  for  $h \in [4, 5]$  and  $j \in [3, 5]$ ).

485 We further leveraged the subject-specific beta-HMMs to compare beta distributions between any HMM  
 486 state in NHP MJ and any HMM state in NHP LM (see Sec. 2.5, Fig. 5(C)). Fig. 5(D) shows the diagonal of  
 487 each of the matrices in Fig. 5(C), and summarizes how each state in NHP MJ compares to the corresponding  
 488 state in NHP LM. In the 40 – 50 Hz range, we found that HMM states 3, 4, and 5 in NHP MJ were most  
 489 similar to the HMM states 3, 4, and 5 in NHP LM, respectively ( $0.40 < Pr(\Delta_{5,jk}^{MJ,LM} \leq 0) < 0.69$  for  
 490  $j \in [3, 5]$  and  $k = j$ ). State 2 in NHP MJ was more similar to state 1 in NHP LM in the 40-50 Hz band  
 491 ( $Pr(\Delta_{5,1,2}^{MJ,LM} \leq 0) = 0.31$ ,  $Pr(\Delta_{5,2,2}^{MJ,LM} \leq 0) = 0.86$ ), while state 2 in NHP LM was more similar to state  
 492 3 in NHP MJ ( $Pr(\Delta_{5,2,3}^{MJ,LM} \leq 0) = 0.42$ ). This indicates that following a ketamine bolus, both NHPs have  
 493 similar activity in the 40-50 Hz band, but that the suppression of gamma activity in state 2 in NHP MJ is  
 494 more prominent than in NHP LM.

495 We found significant differences in the neurophysiological state dynamics between the two primates.  
 496 From the transition matrices, it is apparent that the mean duration in each state in NHP MJ is greater  
 497 than that of NHP LM, indicating faster state-switching dynamics in the latter subject. For NHP MJ, the

<sup>5</sup>See Sec B for a tutorial-styled explanation of how the estimated beta pdf's are used to analyze the spectral properties of the HMM states

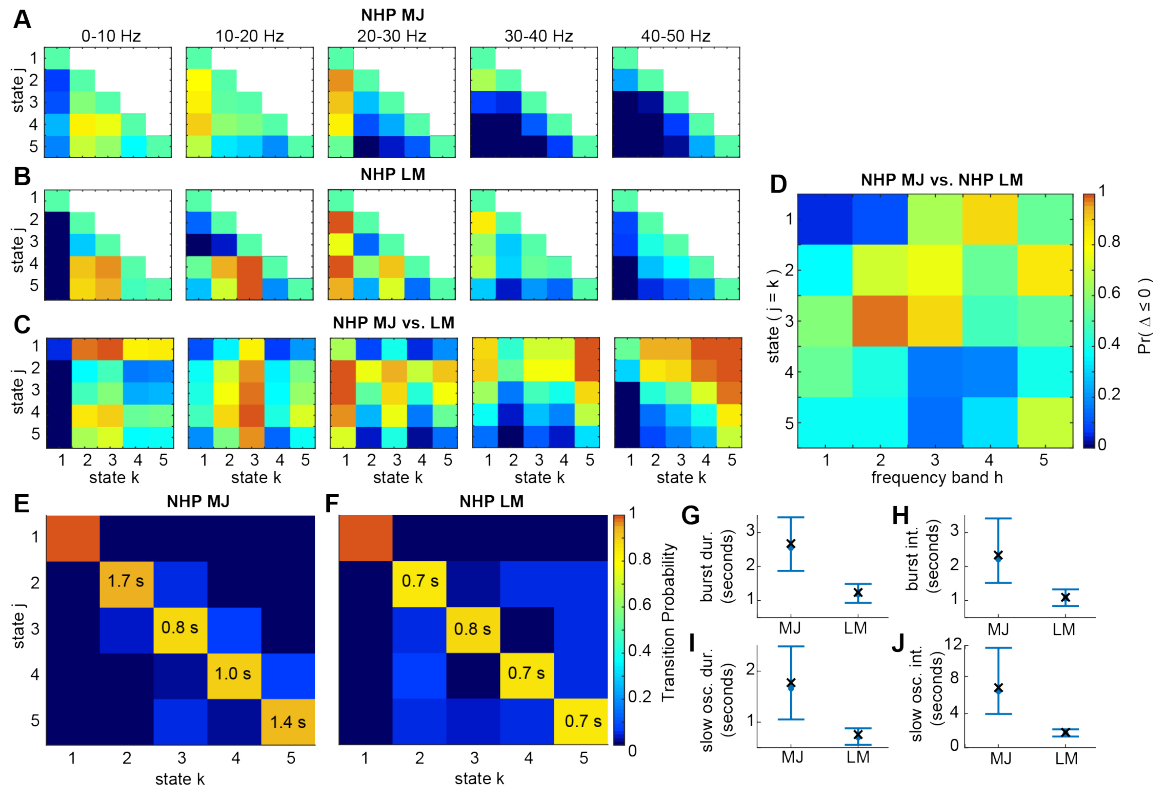


**Figure 5: The estimated beta pdfs and transition matrices characterize the underlying dynamics of NHP LFP data following a 20 mg/kg bolus of ketamine.** (A-C) Heatmaps indicating probability of the event that scaled power in state  $j$  (of NHP MJ in panels A and C, and of NHP LM in panel B) is less than or equal to the scaled power in state  $k$  (of NHP MJ in panel A, and of NHP LM in panels B and C) for  $1 \leq k \leq j \leq 5$  and for each of the 5 frequency bands. The color indicates  $Pr(\Delta \leq 0)$  which represents  $Pr(X_{hj} - X_{hk} \leq 0)$ , where  $X_{hj}$  is a random variable characterized by state  $j$ 's beta pdf in frequency band  $h$  and  $X_{hk}$  is a random variable characterized by state  $k$ 's beta pdf in the same frequency band  $h$ . (D) Heatmap representing diagonal elements from each of the matrices in panel C rearranged columnwise to create a  $5 \times 5$  matrix wherein a row indicates a state pair ( $1 \leq j = k \leq 5$ ) compared between NHP MJ and NHP LM, and a column indicates a frequency band. (E, F) The transition matrices for NHP MJ and NHP LM with expected state duration (in seconds) indicated on the diagonal for all states except the first state. (G-J) Duration statistics corresponding to gamma burst and slow oscillation states in NHP MJ and NHP LM. For each subject, 4000 Markov sequences of length  $N = 2000$  were simulated using the subject-specific estimated transition matrix. The mean duration and interval corresponding to the gamma burst and slow oscillation states were calculated for each realization of these sequences. Median and 95% confidence bounds across all the subject-specific simulated sequences are indicated in blue. The mean duration and interval calculated from the estimated state trajectory (output of the Viterbi algorithm which uses the maximum likelihood beta-HMM parameters and the observations as input) are indicated by a cross ( $\times$ ) symbol.

498 transition matrix revealed that the neurophysiological states switch between the slow oscillation (HMM state  
499 2) and the gamma burst states (HMM states 4 and 5), moving via an intermediate transition state (HMM  
500 state 3). In contrast, for NHP LM, the slow oscillation state is more likely to transition directly to the  
501 gamma burst states and vice versa. The mean duration of the gamma burst state,  $\hat{d}_{4,5}$  (i.e. consecutive  
502 time-windows spent in states 4 or 5), was  $2.5s([1.9, 3.4]s)$  in NHP MJ, and  $1.2s([0.9, 1.5]s)$  in NHP LM. The  
503 mean interval between consecutive occurrences of gamma burst states,  $\hat{d}_{2,3}$ , was  $2.2s([1.5, 3.3])$  in NHP MJ,  
504 and  $1.1s([0.8, 1.3]s)$  in NHP LM. The mean duration of the slow oscillation state,  $\hat{d}_2$ , was  $1.6s([1.1, 2.5]s)$   
505 in NHP MJ, and  $0.7s([0.6, 0.9]s)$  in NHP LM. The mean interval between consecutive occurrences of slow  
506 oscillation states,  $\hat{d}_{3,4,5}$ , was  $6.6s([4.0, 11.9]s)$  in NHP MJ and  $1.7s([1.3, 2.2]s)$  in NHP LM.

#### 507 4.4 Human-specific beta-HMM estimated using observations from multiple pa- 508 tient subjects ( $L > 1$ case)

509 We investigated if the beta-HMM analysis framework could be applied to infer the common ketamine-  
510 induced neurophysiological state dynamics observed in the scalp EEG of multiple OR patients. Therefore,  
511 we fit a single beta-HMM to independently collected EEG data from  $L = 9$  human patients and generated a  
512 quantitative description of ketamine-induced neurophysiological dynamics for a typical patient (Fig. 6). For  
513 this analysis, we chose a model order of  $K = 6$  states, which allowed for classification of broadband high  
514 power, typical of noise artifacts in the OR, as an additional HMM state.

515 As with NHPs, we found that the beta distributions in each frequency band were unique across all states  
516 (KS-distance  $> 0.07$  for all pairwise comparisons; 75 comparisons = 15 pairs of states per frequency band  
517  $\times 5$  frequency bands) (Fig. 6(J); also see Figs. 13 in the Supporting Figures section). We found that HMM  
518 states 4 and 5 had high scaled power in the 30-40 Hz and 40-50 Hz frequency ranges ( $Pr(Y_4 > 0.5|Z =$   
519  $4) = 0.79$ ,  $Pr(Y_4 > 0.5|Z = 5) = 0.99$ ,  $Pr(Y_5 > 0.5|Z = 4) = 0.66$ ,  $Pr(Y_5 > 0.5|Z = 5) = 0.91$ ). We  
520 again considered states 4 and 5 to represent the neurophysiological gamma burst state. There were also  
521 some distinct neurophysiological differences between the human EEG and the NHP LFP. First, there was  
522 a strong slow-oscillation throughout the human EEG recordings, which resulted in more overlap between  
523 the pre-ketamine HMM states and the post-ketamine HMM states in the frontal electrodes. For this reason,  
524 identifying a state dominated by slow activity was less clear in the human beta-HMM model compared  
525 to the NHP beta-HMM models. However, states 1 and 2 had low power in the 30-40 Hz and 40-50 Hz  
526 frequency ranges ( $Pr(Y_4 > 0.5|Z = 1) = 0.00$ ,  $Pr(Y_4 > 0.5|Z = 2) = 0.04$ ,  $Pr(Y_5 > 0.5|Z = 1) = 0.00$ ,  
527  $Pr(Y_5 > 0.5|Z = 2) = 0.21$ ), which is consistent with our definition of the neurophysiological slow oscillation  
528 state, characterized by strong slow activity and low high frequency activity. Second, the gamma bursts in  
529 humans were characterized by a more broadband increase in power – state 5 also had high power in the  
530 10-30 Hz frequency ranges ( $Pr(Y_2 > 0.5|Z = 5) = 0.76$ ,  $Pr(Y_3 > 0.5|Z = 5) = 0.98$ ). Finally, soon after  
531 the time of the ketamine bolus, in patients A, C, E, F, G, and H, there was broadband high power that, in  
532 the context of OR cases, is difficult to distinguish from noise. This activity is classified with the 6-th state,  
533 which also corresponds to periods of obvious noise artifacts (e.g. at  $t = 0$  min in patient D).

534 Further quantitative analysis (Fig. 7) of human EEG beta-HMM parameters revealed high scaled power  
535 in the 30-50 Hz range for the states characterized by gamma burst activity ( $0.00 < Pr(\Delta_{hjk}^H \leq 0) < 0.25$   
536 for  $h \in [4, 5]$ ,  $j \in [4, 5]$  and  $k \in [1, 3]$ ). As previously noted, there was strong slow oscillation activity  
537 throughout the human recordings, and so the changes in 0-10 Hz for states 1-5 were more subtle than in the  
538 NHPs. States 1 and 2 had the lowest power between 30-50 Hz ( $0.00 < Pr(\Delta_{hjk}^H \leq 0) < 0.33$  for  $h \in [4, 5]$ ,  
539  $j \in [3, 5]$ , and  $k \in [1, 2]$ ). Thus, HMM states 1 and 2 best represent the neurophysiological slow oscillation

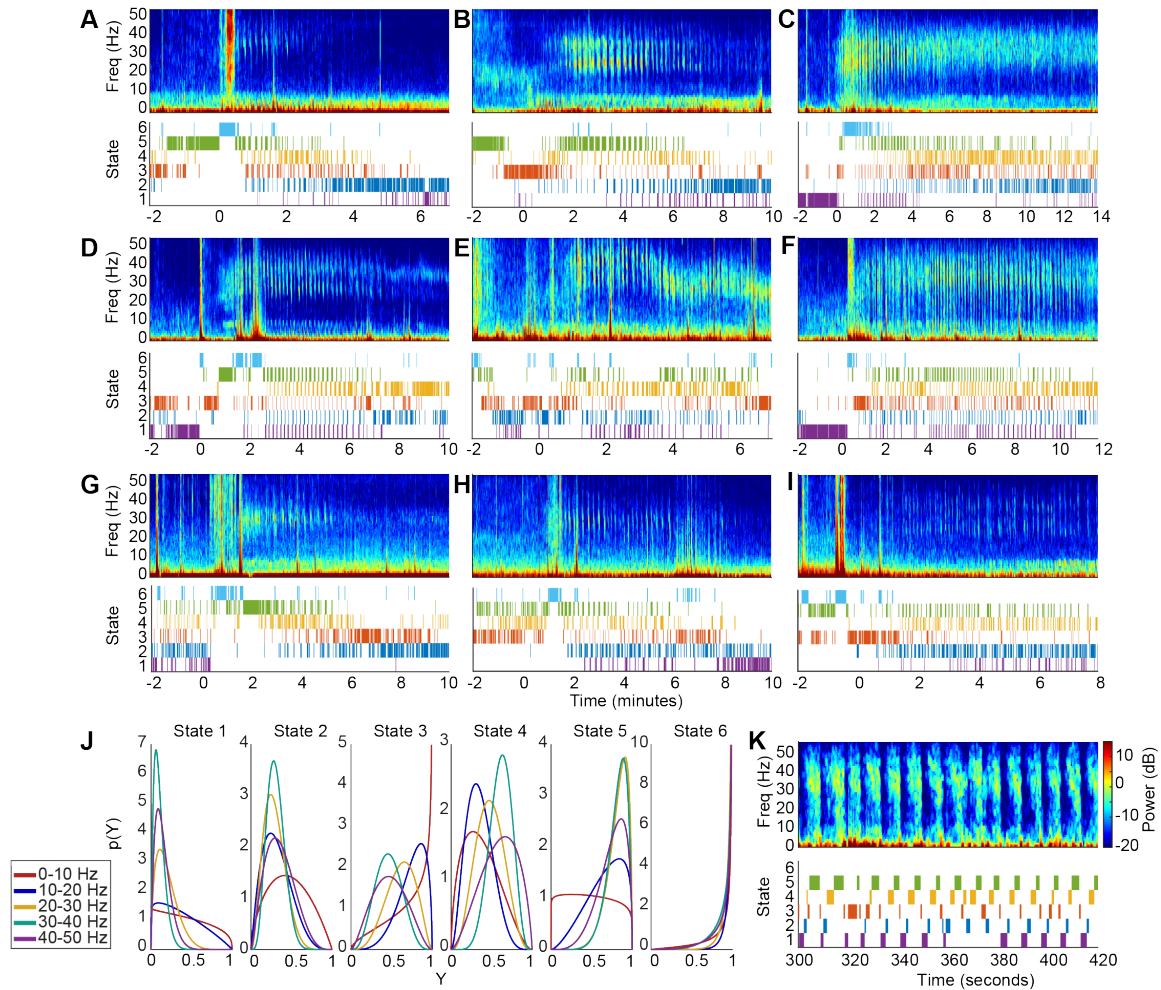
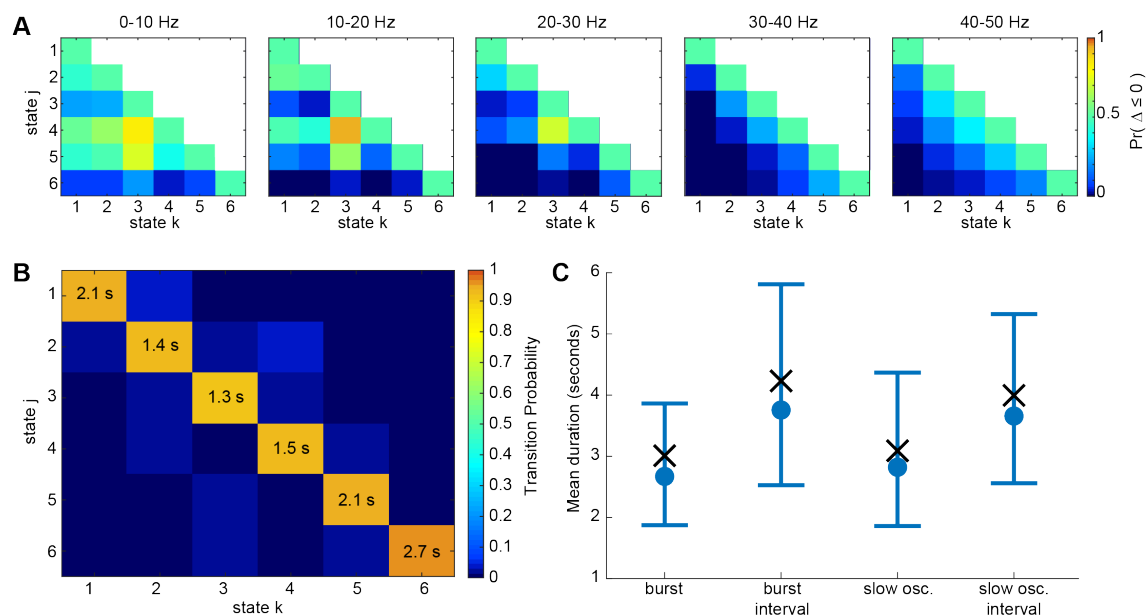


Figure 6: **The 6-state beta-HMM can be fit across independent EEG recordings from multiple human subjects to create a typical human-specific model.** (A-I) Multitaper spectrograms of EEG and corresponding estimated latent state trajectories from 9 human subjects. (J) Frequency band-specific beta pdfs for each of the 6 states estimated from the 9 EEG sessions. (Y - scaled power) (K) Enlarged view of a typical 120s epoch in panel F.



**Figure 7: The estimated beta pdfs and transition matrix characterize the underlying dynamics of human scalp EEG under ketamine-induced general anesthesia.** (A) Heatmaps indicating probability of the event that scaled power in state  $j$  is less than or equal to the scaled power in state  $k$  for  $1 \leq k \leq j \leq 6$  and for each of the 5 frequency bands. The color indicates  $Pr(\Delta \leq 0)$  which represents  $Pr(X_{hj} - X_{hk} \leq 0)$ , where  $X_{hj}$  is a random variable characterized by state  $j$ 's beta pdf in frequency band  $h$  and  $X_{hk}$  is a random variable characterized by state  $k$ 's beta pdf in the same frequency band  $h$ . (B) The transition matrices for NHP MJ and NHP LM with expected state duration (in seconds) indicated on the diagonal for all states. (C) Duration statistics corresponding to gamma burst and slow oscillation states. 4000 Markov sequences of length  $N = 2000$  were simulated using the estimated transition matrix. The mean duration and interval corresponding to the gamma burst and slow oscillation states were calculated for each realization of these sequences. Median and 95% confidence bounds across all the simulated sequences are indicated in blue. The mean duration and interval calculated from the estimated state trajectory (output of the Viterbi algorithm which uses the maximum likelihood beta-HMM parameters and the observations as input) are indicated by a cross (×) symbol.

540 state, characterized by strong slow activity and weak high frequency activity. Finally, through this analysis,  
541 it is again clear that state 6 was characterized by broadband high power ( $0.00 < Pr(\Delta_{h,6,k}^H \leq 0) < 0.25$  for  
542  $h \in [1, 5]$  and  $k \in [1, 5]$ ).

543 Quantitative analysis of the beta-HMM dynamics revealed that the human EEG also tends to transition  
544 cyclically through the HMM states induced by ketamine – the most probable transition sequence, starting  
545 from state 1, is  $1 \rightarrow 2 \rightarrow 4 \rightarrow 5 \rightarrow 3 \rightarrow 2$ . All states have a low probability of transitioning to state 6 ( $A_{j,6} <$   
546  $0.008$  for  $j \in [1, 5]$ ). Furthermore, the mean duration of the gamma burst state,  $\hat{d}_{4,5}$ , was  $2.7s([1.9, 3.8]s)$ . The  
547 mean interval between consecutive occurrences of the gamma burst state,  $\hat{d}_{1,2,3}$ , was  $3.8s([2.5, 5.8]s)$ . The  
548 mean duration of the slow oscillation state  $\hat{d}_{1,2}$  was  $2.8s([1.9, 4.3]s)$ . The mean interval between consecutive  
549 occurrences of slow oscillation state  $\hat{d}_{3,4,5}$  was  $3.6s([2.5, 5.4]s)$ .

## 550 5 Discussion

551 Our beta-HMM analysis framework provided parsimonious summaries of ketamine-induced slow-gamma  
552 alternating dynamics for NHP LFP and human EEG recordings following high-dose ketamine administration.  
553 The input to the analysis framework was one or more sequences of instantaneous power in multiple frequency  
554 bands. The power values were averaged across frequencies within each discrete band and scaled between 0  
555 and 1. The scaling enabled identification of latent HMM states each with a distinct probability distribution  
556 on power values lying between a very low (corresponding to a 0) and a very high value (corresponding  
557 to a 1) in each of the chosen frequency bands, irrespective of the absolute value of spectral estimates. A  
558 key assumption incorporated in the HMM is that at any instant in time, the probability distribution from  
559 which the observation is sampled depends only on the discrete value of an underlying latent state process  
560 at the same instant. This state process itself is assumed to evolve according to a first-order Markovian  
561 transition dynamics. The key outputs of our analysis comprised the model parameters estimated using  
562 an EM algorithm and a corresponding state trajectory estimated using the Viterbi algorithm. The state  
563 trajectory provided an objective and efficient segmentation of LFP and EEG data. The estimated state-  
564 specific and frequency band-specific beta pdf's characterized the spectral representation of each HMM state,  
565 whereas the transition matrix characterized the underlying dynamics. Using the estimated observation pdf's,  
566 we objectively defined neurophysiological states (e.g. gamma burst state, slow oscillation state) in terms of  
567 one or more HMM states. Furthermore, by using the estimated state transition matrices, we calculated mean  
568 duration and mean interval statistics (as defined in Sec. 2.5) corresponding to each of these neurophysiological  
569 states.

570 Our analyses revealed an alternating pattern of states characterized primarily by gamma burst and slow  
571 oscillation activity, as well as intermediate state in between. The mean duration of the gamma burst state  
572 was  $2.5s([1.9, 3.4]s)$  and  $1.2s([0.9, 1.5]s)$  for the two NHPs, and  $2.7s([1.9, 3.8]s)$  for the nine human subjects.  
573 The mean duration of the slow oscillation state was  $1.6s([1.1, 2.5]s)$  and  $0.7s([0.6, 0.9]s)$  for the two NHPs,  
574 and  $2.8s([1.9, 4.3]s)$  for the nine human subjects. Thus, our objective beta-HMM analysis framework enabled  
575 us to precisely characterize the dynamics of ketamine-induced gamma burst and slow oscillation states, and  
576 to compare the time-scales of these neurophysiological states between subjects and between species.

577 Our work advances the development and application of LFP or EEG data analysis tools. The beta-HMM  
578 analysis framework falls under the broad category of research aimed at developing time-frequency state space  
579 models to analyze neural dynamics [41, 50, 64, 65, 66, 67], and applying them in principled interpretation  
580 of neural time-series data for unconsciousness research [12, 64]. A few key distinguishing features of the

581 beta-HMM analysis framework are as follows. The assumption of state-specific and frequency-band specific  
582 beta distributions as marginal distributions of the instantaneous observation vectors allows for a flexible  
583 framework to characterize highly variable spectral profiles. This assumption, along with the assumption of  
584 Markovian state transitions, allowed us to directly characterize the discontinuous switching among multiple  
585 spectral profiles, as well as identify segments with similar spectral properties (See figures 3 C, D; 4 F, M; and  
586 6 K). Furthermore, our beta-HMM analysis framework accounts for the disjoint nature of data from separate  
587 sessions without requiring any concatenation of sessions or consequently any arbitrary choice of concatenation  
588 order. Potential extensions of this work on the statistical methods development front may include modeling  
589 the transition matrix as time-varying, which would account for longer time-scale variations (e.g. varying drug-  
590 levels). Furthermore, generalizing the current single-channel LFP or EEG data-based analysis framework to  
591 incorporate multi-channel LFP or EEG data would allow for neurophysiological characterization of ketamine-  
592 induced altered arousal states based on spatio-temporal statistical relationships in the observed data. Going  
593 beyond the context of ketamine-induced altered arousal states, the analysis framework itself can be relevant  
594 in general use-cases where LFP or EEG data demonstrate discontinuous, repeating transitions among time-  
595 limited, band-limited spectral signatures, such as those observed during sleep [41, 68] or burst suppression in  
596 general anesthesia [69, 70]. In such applications, it will also be straight forward to modify the definitions of  
597 frequency bands in our work to incorporate frequency bands conventionally adopted in neuroscience studies  
598 [11, 71]<sup>6</sup>.

599 Our beta-HMM research can inform future neuroscience inquiries. While there are several hypotheses  
600 for the generation of gamma activity under ketamine [19], there is not yet a clear understanding of how the  
601 bursting activity is generated. Preliminary work indicates that there may be a cycle of cortical inhibition and  
602 dis-inhibition due to activity-dependent ketamine NMDAR inhibition of cortical interneurons and pyramidal  
603 neurons [20]. Our analyses of the NHP datasets using the beta-HMM led to the identification of neurophys-  
604 iological states that were primarily associated with the period following administration of a ketamine bolus.  
605 The summary statistics from each NHP inform *which* frequency bands show significant activity, and *how* this  
606 activity varies over time. The duration and interval statistics of the alternating gamma burst state, and the  
607 slow oscillation states that we estimated for NHP LFP can serve as quantitative constraints in the design of  
608 rhythm-generating neuronal microcircuit models that would mimic the neurophysiological dynamics caused  
609 by ketamine, similar to ones previously done for other anesthetics [21, 22, 24, 72, 73]. Furthermore, we  
610 identified a previously unreported transition state between the alternating gamma burst and slow oscillation  
611 states, and a mechanistic characterization of this state would complement ongoing statistical analyses of  
612 neurophysiological data.

613 Our beta-HMM research can also inform future clinical inquiries. Ketamine is known to produce distinct  
614 oscillatory signatures in the electroencephalogram (EEG) of healthy volunteers and patients [10, 11]. These  
615 oscillatory signatures are starkly different from those produced during propofol-induced unconsciousness  
616 [71, 74]. These differences in oscillatory dynamics, particularly the presence of alternating slow oscillation  
617 and gamma burst states under ketamine, indicate that a spectral marker of propofol-induced unconsciousness  
618 is not a reliable marker for tracking ketamine-induced altered arousal states. However, the existence of  
619 consistent neurophysiological states observed in EEG following ketamine bolus administration in multiple  
620 patients indicate promise in precise monitoring of these states to track ketamine-induced altered states of  
621 arousal. Towards this goal, as demonstrated in this work, the beta-HMM analysis framework can provide

---

<sup>6</sup>Reiterating, the motivation for our choice of frequency bands in this work was to maintain consistency and objectivity in our analyses across the multiple NHP LFP and human EEG datasets.

622 precise, objective characterization of the neurophysiological dynamics associated with ketamine-induced  
623 altered states of arousal. Furthermore, in addition to its use for general anesthesia and analgesia, ketamine  
624 is also used in treatment of depression [75, 76] and in pharmacologic models for schizophrenia [18, 77, 78].  
625 Thus the clinical utility and mechanistic insights gained by detailed quantification of the neural activity  
626 corresponding to ketamine-induced altered states of arousal can potentially aid future research and clinical  
627 applications.

628 There are two primary limitations in both the data set that we analysed here and in our assumptions. The  
629 first limitation is a need for prospective studies in humans and animals with carefully recorded simultaneous  
630 neural, behavioral response and physiological activities. Future experimental studies with larger cohorts can  
631 address the current study’s limitation due to low number of subjects in both the NHP LFP and human  
632 EEG analyses. The consistency of the alternating gamma-slow spectral activity from 9 patients and 2 NHPs  
633 during ketamine-induced altered arousal states indicate that transition dynamics between the gamma burst  
634 and slow-delta neurophysiological states can be a candidate biomarker of ketamine-induced unconsciousness.  
635 However, to reliably establish these EEG or LFP correlates of unconsciousness, experimental studies in  
636 healthy volunteers and animal subjects with simultaneous monitoring of behavioral response, physiological  
637 parameters and neural activity will be essential. The second limitation is a need for extension to real-  
638 time tracking of neurophysiological states during ketamine-induced general anesthesia. While our current  
639 approach utilizes the entire data set to calculate appropriate scaling factors for transforming spectral power  
640 to real numbers lying between 0 and 1, and thus (in the present formulation) cannot be executed in real  
641 time. A larger study may allow for the development of a generalized scaling approach. This would facilitate  
642 objective identification of ketamine neurophysiological states in real-time. While a common limitation of  
643 EEG analysis in real-time OR settings is the presence of motion and other noise artifacts in recordings,  
644 the beta-HMM framework is well poised to handle these artifacts, as observations that fall far outside the  
645 distribution of the signal can be assigned to a distinct HMM state.

646 In conclusion, we have developed a detailed analysis framework for ketamine-induced neurophysiological  
647 phenomena. The generalizability of the beta-HMM framework indicates utility beyond what has been re-  
648 ported here. Future work will investigate how the spectral dynamics revealed by our analysis contribute to  
649 ketamine-induced altered states of arousal.

## 650 **6 Acknowledgement**

651 The authors thank Prof. Polina Anikeeva for her feedback throughout the manuscript preparation and Dr.  
652 Alexis Garcia for suggesting helpful references.

## 653 **7 Funding Sources**

654 This work was partially supported by NIH Award P01-GM118629 (to E. N. Brown, E. K. Miller), NIH Award  
655 R01MH115592 (to E. K. Miller), NIH Award 5T32EB019940-05 (to I. C. Garwood), NSF GRFP (to I. C.  
656 Garwood), funds from Massachusetts General Hospital (to E. N. Brown), funds from the Picower Institute  
657 for Learning and Memory (to E. N. Brown), Picower Postdoctoral Fellowship (to S. Chakravarty).

## 658 8 Author Contributions

659 **Conceptualization:** S. Chakravarty, I. C. Garwood, E. N. Brown

660 **Formal Analysis:** I. C. Garwood, S. Chakravarty, E. N. Brown

661 **Funding Acquisition:** E. N. Brown

662 **Investigation:** I. C. Garwood, S. Chakravarty, J. Donoghue, O. Akeju

663 **Methodology:** I. C. Garwood, S. Chakravarty

664 **Software:** I. C. Garwood, S. Chakravarty

665 **Resources:** E. K. Miller, O. Akeju, E. N. Brown

666 **Data Curation:** I. C. Garwood, J. Donoghue, S. Chamadia, O. Akeju, P. Kahali

667 **Supervision:** E. N. Brown

668 **Visualization:** I. C. Garwood

669 **Writing-Original Draft:** I. C. Garwood, S. Chakravarty

670 **Writing-review & editing:** I. C. Garwood, S. Chakravarty, E. N. Brown, E. K. Miller, S. Chamadia, O.

671 Akeju, J. Donoghue, P. Kahali

## 672 A M-step of EM

We calculate  $\Theta^{(n)}$  by solving the constrained maximization of the  $Q(\Theta, \hat{\Theta})$  (Eq. (8)) ,

$$\max_{\Theta} Q(\Theta, \hat{\Theta}) \text{ such that,} \quad (16)$$

Equality constraints:

$$\sum_{k=1}^K A_{jk} = 1 \quad \forall k \in [1, K] \quad (17)$$

$$\sum_{k=1}^K \pi_{k,l} = 1 \quad \forall l \in [1, L], \quad (18)$$

Inequality constraints:

$$- \pi_{k,l} \leq 0 \quad \forall k \in [1, K], l \in [1, L] \quad (19)$$

$$- A_{jk} \leq 0 ; \quad \forall j, k \in [1, K] \quad (20)$$

$$- (a_{hk}^2 + b_{hk}^2 - 2) \leq 0 \quad \forall h \in [1, H], k \in [1, K] \quad (21)$$

Due to the independent additive contributions to the objective function due to each group of decision variables,  $\pi_{k,l}$ ,  $\{\mathbf{A}\}$  and  $\{a_{hk}, b_{hk}\}_{h=1, k=1}^{H, K}$ , we seek to increase  $Q(\Theta, \hat{\Theta})$  by maximizing these individual

contributions independently. To implement this we solve the following optimization problems,

$$\hat{\pi}_l = \arg \max_{\pi_l} \sum_{k=1}^K \gamma_{1,l}(k) \log \pi_{k,l} \text{ , such that } \sum_{k=1}^K \pi_{k,l} = 1, \pi_{k,l} \geq 0 \quad (22)$$

$$\begin{aligned} \{\hat{A}_{jk}\}_{k=1}^K &= \arg \max_{\{A_{jk}\}_{k=1}^K} \sum_{l=1}^L \sum_{n=1}^{N_l} \sum_{j=1}^K \sum_{k=1}^K \xi_{n,l}(j, k) \log A_{jk} \\ &= \arg \max_{\{A_{jk}\}_{k=1}^K} \sum_{l=1}^L \sum_{n=1}^{N_l} \sum_{k=1}^K \xi_{n,l}(j, k) \log A_{jk} \\ &\text{such that } \sum_{k=1}^K A_{jk} = 1, A_{jk} \geq 0 \end{aligned} \quad (23)$$

$$\begin{aligned} \{\hat{a}_{hk}, \hat{b}_{hk}\} &= \arg \max_{\{a_{hk}, b_{hk}\}} \sum_{l=1}^L \sum_{n=1}^{N_l} \sum_{k=1}^K \sum_{h=1}^H \gamma_{n,l}(k) \log Pr(y_{nh,l} | z_{n,l} = k; a_{hk}, b_{hk}) \\ &= \arg \max_{\{a_{hk}, b_{hk}\}} \sum_{l=1}^L \sum_{n=1}^{N_l} \gamma_{n,l}(j) \log Pr(y_{nh,l} | z_{n,l} = k; a_{hk}, b_{hk}) \text{ ,} \\ &\text{such that } a_{hk}^2 + b_{hk}^2 - 2 > 0 \end{aligned} \quad (24)$$

Note that in Eqs. (22), (23) and (24) we are solving for 1,  $K$  and  $KH$  independent optimization problems. The solutions to Eq. (22) and the (23) has the following closed-form expressions,

$$\hat{\pi}_{k,l} = \gamma_{1,l}(k) \text{ ,} \quad (25)$$

$$\hat{A}_{jk} = \frac{\sum_{l=1}^L \sum_{n=1}^{N_l} \xi_{n,l}(j, k)}{\sum_{k=1}^K \sum_{l=1}^L \sum_{n=1}^{N_l} \xi_{n,l}(j, k)} \quad (26)$$

673 To solve the constrained optimization problem in Eq. (24), we use the Lagrange multiplier method [79].  
 674 Alternatively, we can directly employ numerical tools for constrained optimization such as the `fmincon`  
 675 function in Matlab.

## 676 B Tutorial on analyzing HMM state-specific spectra in terms of 677 corresponding estimated beta pdf's

678 Here we present a tutorial-styled discussion on how to use HMM state-specific frequency band-specific beta  
 679 pdf's (estimated using EM algorithm described in Sec. 2.4) to interpret the corresponding HMM state-specific  
 680 spectral profiles. To demonstrate the utility of the state-specific beta distributions, we use segmented data  
 681 from the 2 HMM states, states 2 and 5, identified in the single session analysis of NHP LFP data (Fig. 3). To  
 682 elucidate the correspondence between the spectral profile (Fig. 8(A, B) and Fig. 8(E,F)) and the respective  
 683 empirical pdfs of the scaled powers (Fig. 8(C) and Fig. 8(G)), we recall the intuition provided in Sec 2.2  
 684 with regard to the scaling equation (Eq. (2)). Recall that the scaling factor for each frequency band is  
 685 calculated from the quartiles of the spectrogram across the entire session. As a result, if the distribution  
 686 of spectral power corresponding to a given state and frequency band has a similar variance to that of the

entire session, its scaled representation will have high variance. This will correspond to a relatively flat beta distribution. In contrast, if the spectral power from a given state and frequency band tends to be greater than the median of the corresponding frequency band, the scaled observations will be skewed towards 1. Particularly, if the observations corresponding to a given HMM state are mostly between the third and fourth quartile, the pdf of the beta distribution for that state will have high probability mass between 0.75 and 1. Note that corresponding statements can be made for states with relatively lower spectral power in a given frequency band (i.e., the beta distributions would be skewed towards 0). We use this intuition to quantitatively characterize the spectral power in a given frequency band for states 2 and 5.

As seen in Fig. 8(A,B), there is prominent power in the 0-10 Hz band for state 2. These power values are higher than the median value across the entire session, as indicated by high probability mass near 1 in Fig. 8(C). This right shift of the probability mass towards 1 in the scaled power pdf's is also represented by a high complementary cdf (ccdf)<sup>7</sup> at 0.5 (Fig. 8(D)) with  $Pr(Y_1 > 0.5|Z = 2) = 0.82$ . In state 2, there is not much activity in the 10-20 Hz band (Fig. 8(B)). This is similar to the activity across the majority of the session, and so the distribution of the scaled power has high variance (Fig. 8(C); our analysis of all the states in Fig 3 also show that 10-20 Hz power is not a discriminating feature across the states). In state 2, there is not much activity in the 20-30Hz, 30-40 Hz, and 40-50 Hz bands (Fig. 8(B)), and the power values are mostly lower than the median (as indicated by high probability mass near 0 in Fig. 8(C)). The left shift of the probability mass towards 0 in the scaled power is also represented by the low ccdf values at 0.5 (Fig. 8(D)) with  $Pr(Y_3 > 0.5|Z = 2) = 0.002$ ,  $Pr(Y_4 > 0.5|Z = 2) = 0.002$ , and  $Pr(Y_5 > 0.5|Z = 2) = 0.004$ .

Now using the intuitions built from our discussion of state 2, let us try to interpret the spectral representation of state 5. In the 0-10 Hz band there is prominent activity in state 5 (Fig. 8(E,F)), but the high variance of the distribution of scaled power (Fig. 8(G)) indicates that the variance of the unscaled power from state 2 is similar to the variance across the entire session. In 10-20 Hz band there is not much activity in state 5 (Fig. 8(F)), but the power values tend to be higher than the median value of the entire session (as indicated by the large spread but a mode  $> 0.5$  in Fig. 8(G)). In each of the 20-30Hz, 30-40Hz, 40-50Hz bands there is prominent activity (Fig. 8(E,F)), and the large probability mass near 1 in the scaled power pdf's (Fig. 8(G)) indicates that these activities are higher than the respective median values. This right shift is clearly captured by the ccdf values at 0.5 -  $Pr(Y_3 > 0.5|Z = 5) = 0.98$ ,  $Pr(Y_4 > 0.5|Z = 5) = 1.00$ , and  $Pr(Y_5 > 0.5|Z = 5) = 0.97$ .

We can further use these beta pdfs to quantitatively compare the power values in a given frequency band between states 2 and 5. Using the Eq. (9), we define a  $\Delta_{h,5,2} = X_{h,5} - X_{h,2}$ , such that  $X_{h,5} \sim Beta(a_{h,5}, b_{h,5})$  and  $X_{h,2} \sim Beta(a_{h,2}, b_{h,2})$ . Fig. 8(I) and Fig. 8(J) represent the pdf and cdf for the  $\Delta_{h,5,2}$  where  $h \in [1, 5]$ . For bands 0-10 Hz and 10-20 Hz, most of the probability mass on  $\Delta_{h,5,2}$  lies around 0 and the corresponding CDF values at 0 (which correspond to  $Pr(\Delta_{h,5,2} \leq 0)$ ) are 0.70 and 0.34, respectively. This indicates that while state 2 tends to have higher power in the 0-10 Hz band and state 5 tends to have higher power in the 10-20 Hz band, the activity in these bands is most likely not a significant discriminating factor between the two states. However, for the bands 20-30Hz, 30-40Hz, 40-50Hz, most of the probability mass of the respective  $\Delta$ 's occurs to the right of 0, which results in CDF values at 0 of 0.01,  $1.9 \times 10^{-5}$  and  $1.1 \times 10^{-4}$ , respectively. This indicates that the power in these three frequency bands is higher in state 5 compared to state 2, and the activity in these bands is likely to be significant discriminating factor between the two states. Thus we can generate a quantitative description to support our qualitative assessment that in high frequency bands, state 5 has higher power relative to state 2.

<sup>7</sup>ccdf at a given sample point equals 1 minus the value of the cdf at the same sample point

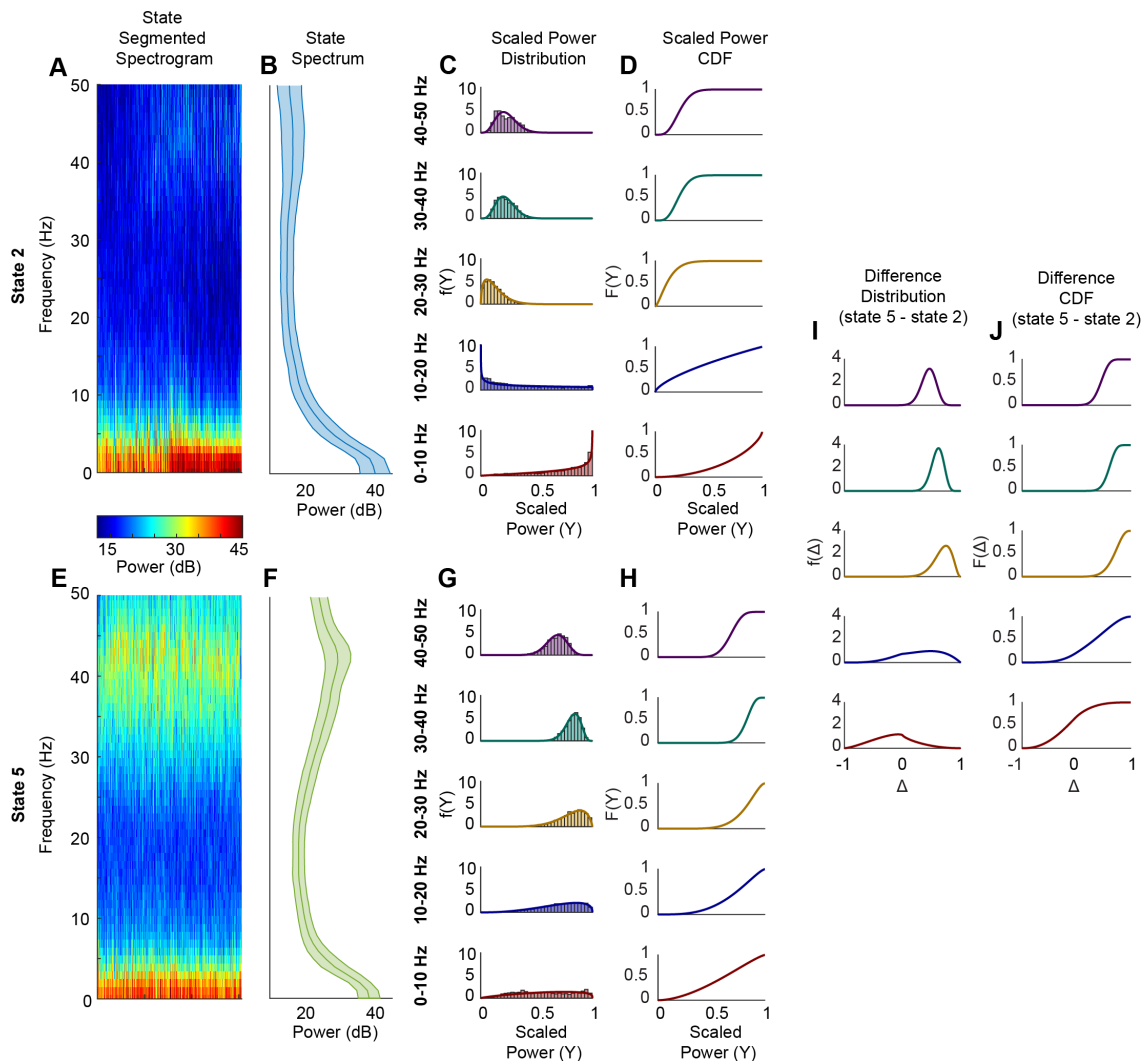


Figure 8: Illustrative example of how to interpret the state-specific spectral profiles in terms of the state-specific frequency-band specific beta pdf's. (A, E) Group of spectra from time-points identified as states 2 and 5 (by the Viterbi algorithm), respectively, of a 5 state beta-HMM fitted to a single session of NHP data. (B,F) The average and standard deviation across all the spectral profiles for states 2 and 5, respectively. (C, G) Empirical pdfs of the scaled power in the 5 frequency bands, based on the data from the time-points identified as states 2 and 5 (by the Viterbi algorithm), respectively. The state-specific frequency-band specific beta pdfs of the maximum likelihood beta-HMM (estimated by the EM algorithm) is overlaid. (D, H) The cdf corresponding to the estimated beta pdfs plotted in C and G, respectively. (I) The frequency-band specific pdf of the difference random variable  $\Delta = X_{h,5} - X_{h,2}$ , where  $X_{h,5} \sim Beta(a_{h,5}, b_{h,5})$  and  $X_{5,h} \sim Beta(a_{h,2}, b_{h,2})$  based on the respective estimated pdfs, (J) The cdf corresponding to the frequency band-specific pdf's in (I).

729 **C Supporting figures and table**

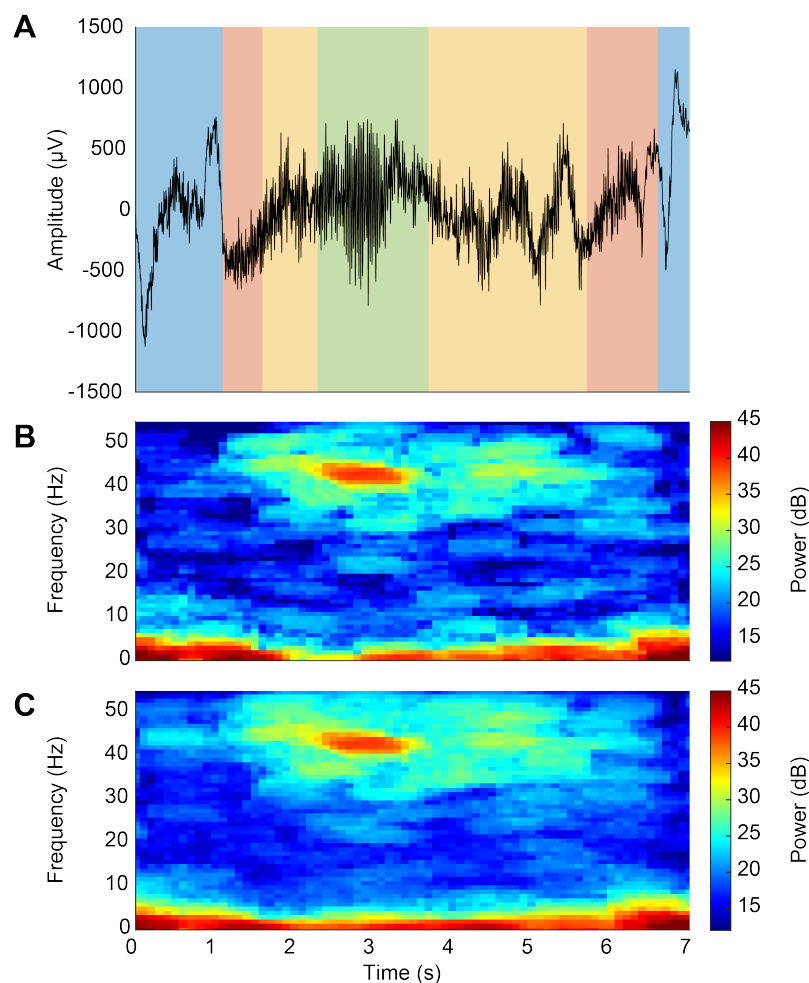


Figure 9: A typical 7 second epoch (following a high-dose ketamine bolus) of LFP from a single electrode of a multi-electrode array located in the PFC (area 8A) of NHP MJ is presented in panel A. Time 0 corresponds to 743.5 seconds after the bolus was administered. We fit our beta-HMM to the reduced-order representation (derived using Eqs (1) and (2)) of the corresponding multitaper spectrogram, presented in panel B. The resulting optimal segmentation is represented by the colored vertical bars overlaid on the neural time-series in panel A. State 2 is shown in blue, state 3 in red, state 4 in yellow, and state 5 in green. (State 1, which corresponds to the time before the ketamine bolus, is not shown here.) Panel C represents the average spectrogram across all the electrodes in the same multi-electrode array.

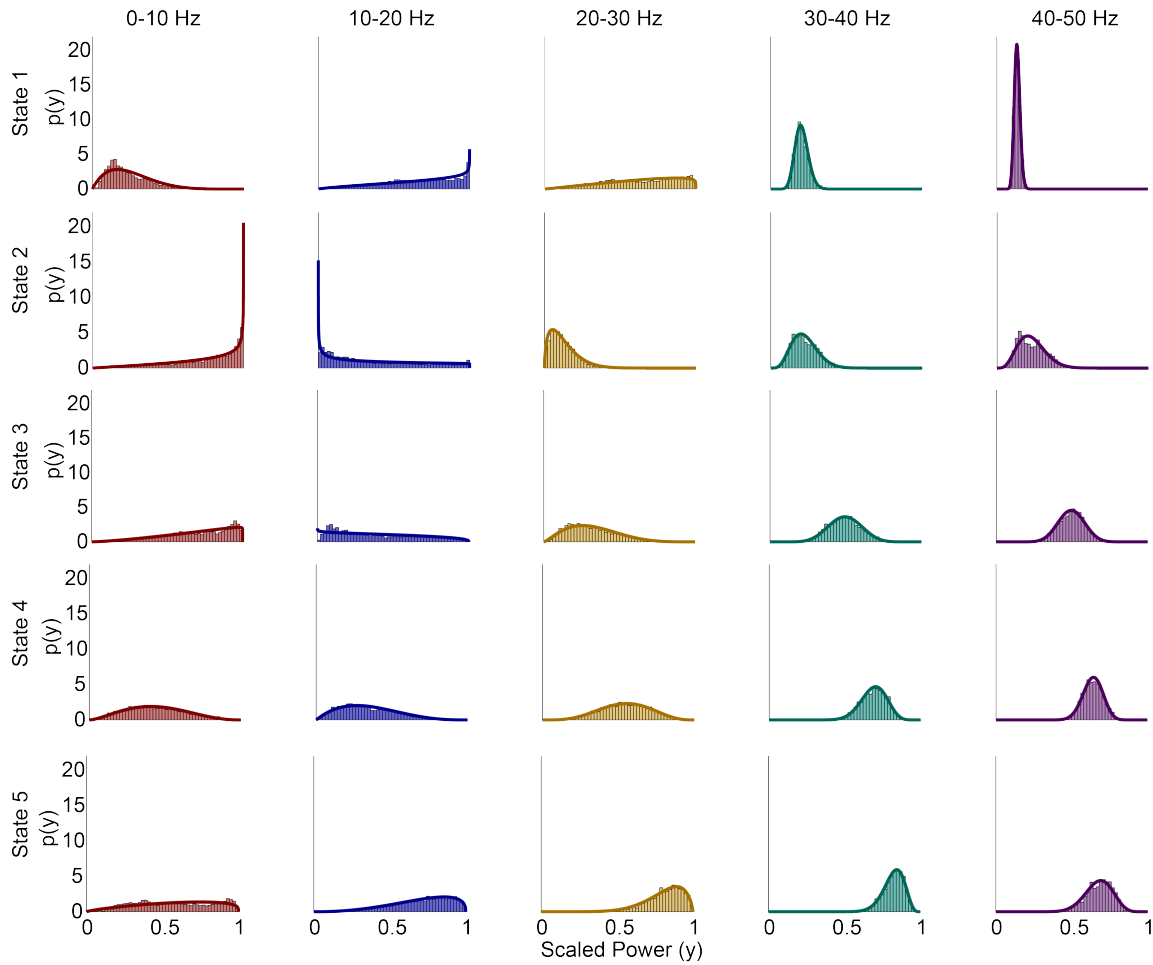


Figure 10: Illustration of the state-specific and frequency-band specific beta pdfs corresponding to a 5-state beta-HMM that is estimated from  $L = 1$  session of LFP recording from NHP MJ. For each state (viewed row-wise) and a frequency band (viewed column-wise), the corresponding subplot presents (1) the empirical pdf plotted as a histogram based on the observations that correspond to the optimal segmentation of the data sequence, and (2) the continuous beta pdf with parameters estimated by the EM algorithm. Each color distinguishes a frequency band.

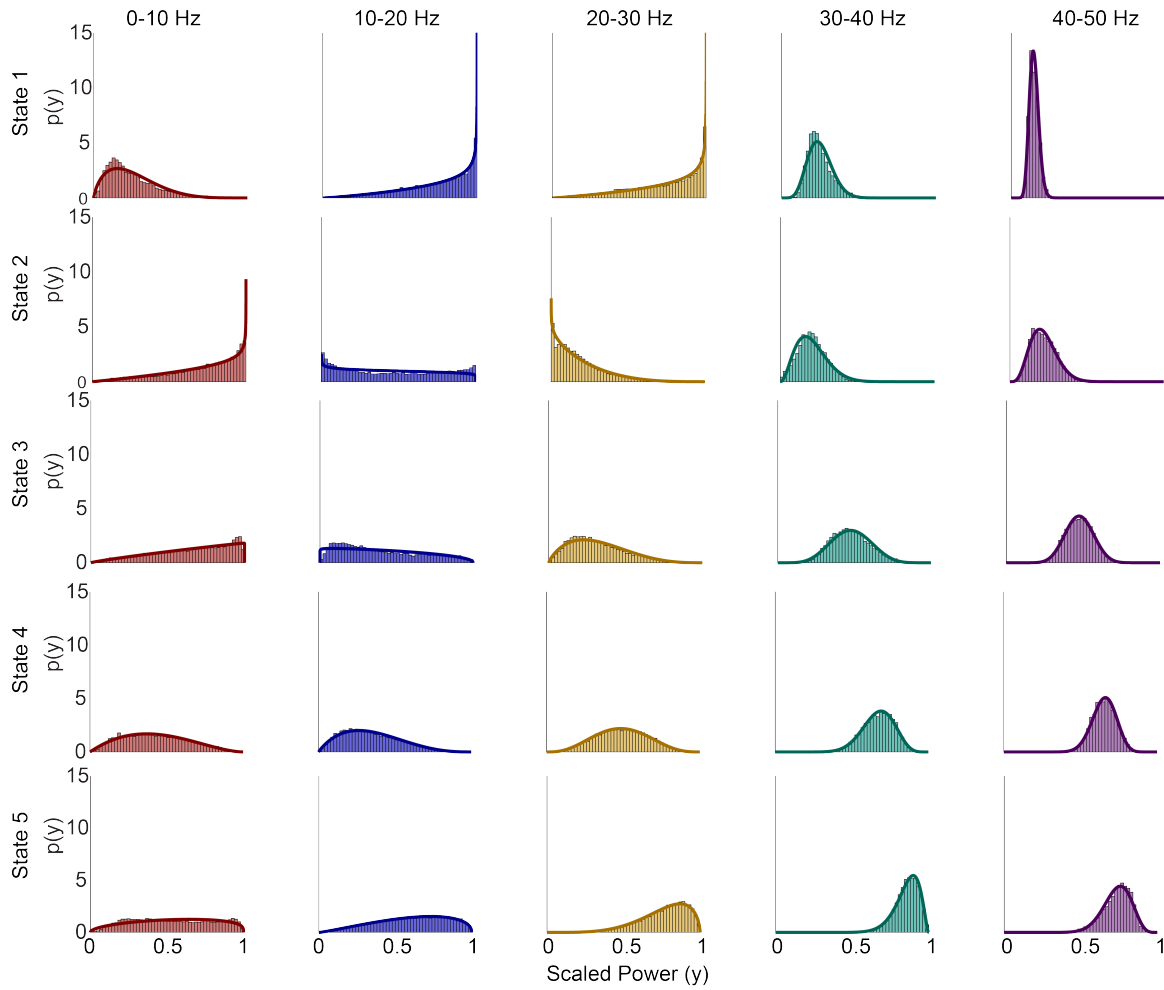


Figure 11: Illustration of the state-specific and frequency-band specific beta pdfs corresponding to a 5-state beta-HMM that is estimated from  $L = 4$  sessions of LFP recording from NHP MJ. For each state (viewed row-wise) and a frequency band (viewed column-wise), the corresponding subplot presents (1) the empirical pdf plotted as a histogram based on the observations that correspond to the optimal segmentation across the  $L=4$  sessions, and (2) the continuous beta pdf with parameters estimated by the EM algorithm. Each color distinguishes a frequency band.

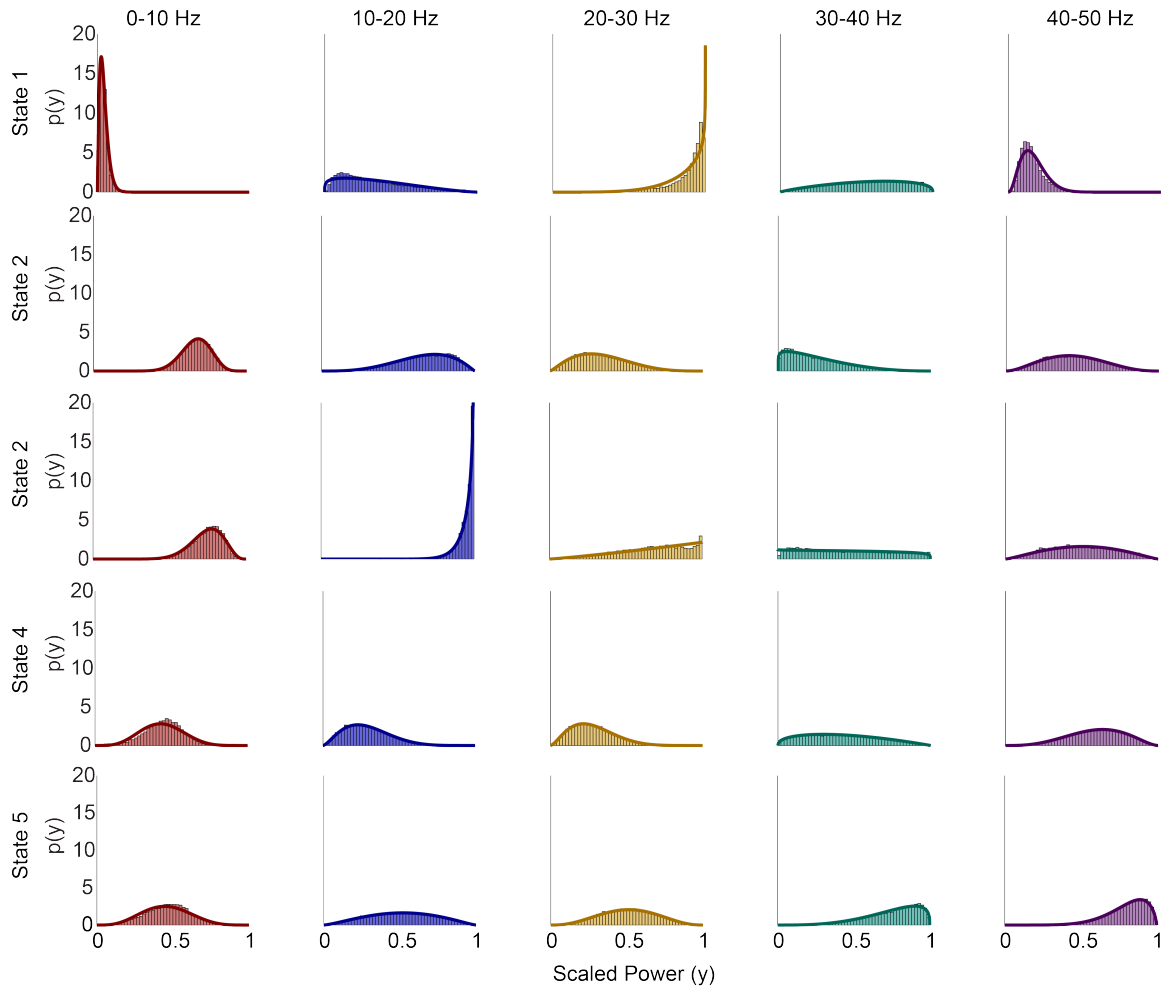


Figure 12: Illustration of the state-specific and frequency-band specific beta pdfs corresponding to a 5-state beta-HMM that is estimated from  $L = 5$  sessions of LFP recording from NHP LM. For each state (viewed row-wise) and a frequency band (viewed column-wise), the corresponding subplot presents (1) the empirical pdf plotted as a histogram based on the observations that correspond to the optimal segmentation across the  $L=5$  sessions, and (2) the continuous beta pdf with parameters estimated by the EM algorithm. Each color distinguishes a frequency band.

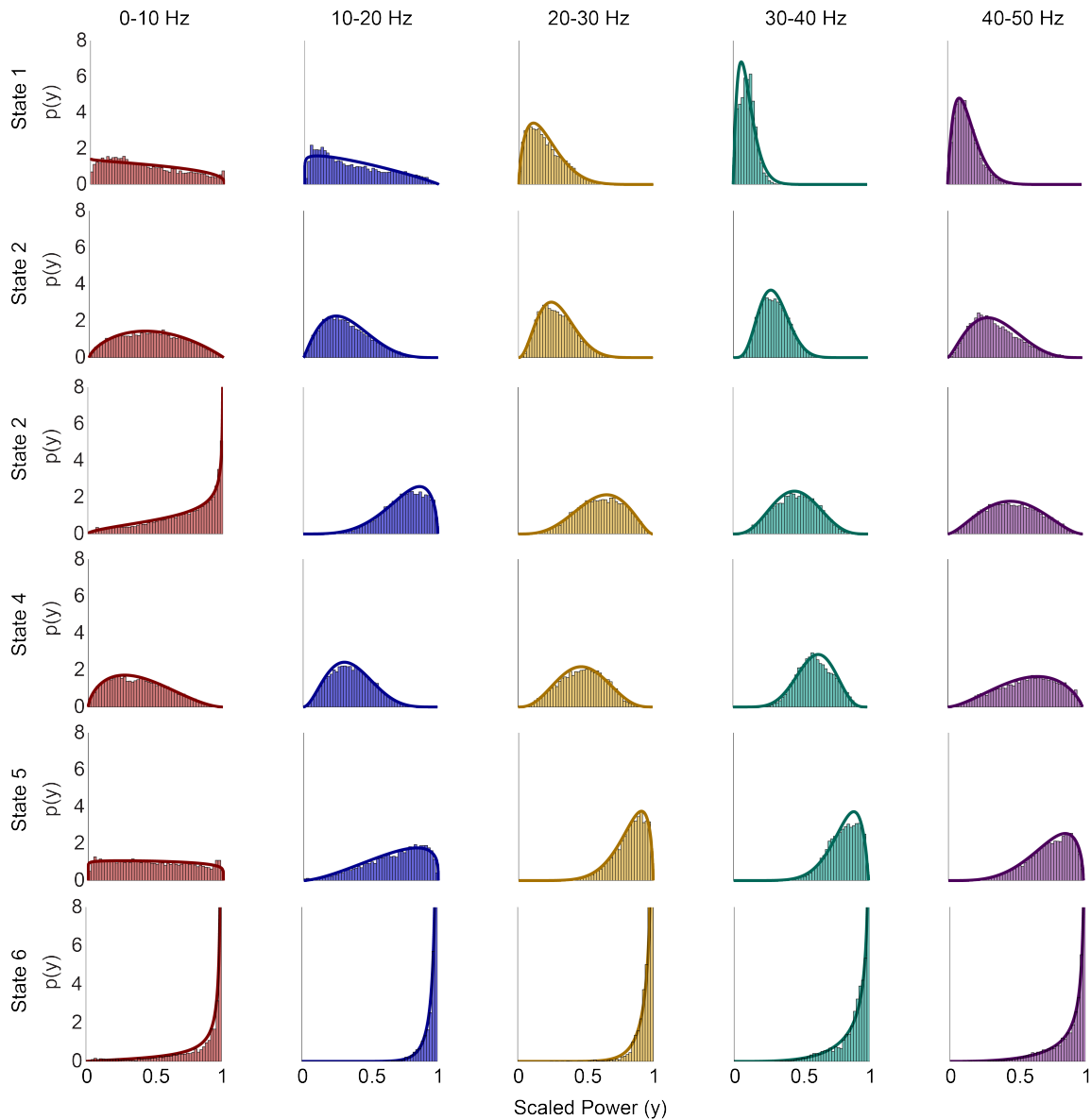


Figure 13: Illustration of the state-specific and frequency-band specific beta pdfs corresponding to a 6-state beta-HMM that is estimated from  $L = 9$  sessions of EEG recording from 9 human OR patients. For each state (viewed row-wise) and a frequency band (viewed column-wise), the corresponding subplot presents (1) the empirical pdf plotted as a histogram based on the observations that correspond to the optimal segmentation across the  $L=9$  sessions, and (2) the continuous beta pdf with parameters estimated by the EM algorithm. Each color distinguishes a frequency band.

Table 2: Algorithm to simulate data from an NHP LFP session with an underlying Markovian latent state path for numerically testing the beta-HMM framework

<b>Input</b>	Spectrogram $\{S_n(\omega_i)\}_{n=1}^N$ (for every frequency $\omega_i \in \{\omega_r, 2\omega_r, \dots, 50\}$ ) from one LFP recording session from NHP MJ of duration 20 min, user-specified number of states $K$ and HMM parameters $\boldsymbol{\pi}$ and $\mathbf{A}$ , and length of session to simulate, $M = 12000$ .
1	Calculate $\{\bar{S}_n(\boldsymbol{\omega})\}_{n=1}^N$ (Eq. 1).
2	Identify $K$ distinct clusters of spectra by executing a k-means clustering algorithm ([31]) on $\{\bar{S}_n(\boldsymbol{\omega})\}_{n=1}^N$ . Label each cluster from 1 to $K$ in ascending order of within-cluster mean power in the 40-50 Hz frequency band. Note: Each time-point $n$ is now associated with a cluster label 1 to $K$ .
3	Store the original time-point indices corresponding to each element in $k$ -th cluster in an integer-valued set $\mathbf{n}_k$ , where $k \in [1, K]$ . Note: $\bigcup_{k=1}^K \mathbf{n}_k = [1, N]$ and $\bigcap_{k=1}^K \mathbf{n}_k = \emptyset$ , where $\emptyset$ denotes the null set.
4	Simulate a state path by generating a Markov sequence $\{z_m\}_{m=1}^M$ using the set of parameters $\{\boldsymbol{\pi}, \mathbf{A}\}$ .
5	Simulate an LFP spectrogram, $\{S_m^{sim}(\cdot)\}_{m=1}^M$ , as follows: when $z_m = k$ , uniformly sample index $n_k$ from $\mathbf{n}_k$ , and set $S_m^{sim}(\omega_i) = S_{n_k}(\omega_i)$ for every frequency $\omega_i \in \{\omega_r, 2\omega_r, \dots, 50\}$ . Also, set the frequency band-specific average of the simulated spectrum corresponding to $z_m = k$ , $\bar{S}_m^{sim}(\boldsymbol{\omega}) = \bar{S}_{n_k}(\boldsymbol{\omega})$ .
6	Calculate $\mathbf{Y} = \{\mathbf{y}_m\}_{m=1}^M$ using $\{\bar{S}_m^{sim}(\boldsymbol{\omega})\}_{m=1}^M$ (Eq. 2).
7	Determine cluster-specific and frequency-band specific maximum-likelihood estimate of the beta distribution parameters, $\{a_{hk}, b_{hk}\}$ , for all $h = \{1, 2, \dots, H\}$ and $k = \{1, 2, \dots, K\}$ from $\mathbf{Y}$ . Note: $\boldsymbol{\phi} = \{\{a_{hk}, b_{hk}\}_{h=1}^H\}_{k=1}^K$ estimated based on the simulated state path is considered as <i>ground truth</i> for the purpose of numerically testing the beta-HMM estimation framework.
<b>Output</b>	$\{S_m^{sim}(\omega_i)\}_{m=1}^M$ (for every frequency $\omega_i \in \{\omega_r, 2\omega_r, \dots, 50\}$ ) and corresponding $\mathbf{Y}$ , $\{z_m\}_{m=1}^M$ , and $\boldsymbol{\phi}$ .

## References

- 730
- 731 [1] Edward F. Domino, Peter Chodoff, and Guenter Corssen. Pharmacologic effects of ci-581, a new  
732 dissociative anesthetic, in man. *Clinical Pharmacology & Therapeutics*, 6(3):279–291, 1965.
- 733 [2] M.D. Domino, Edward F. Taming the Ketamine Tiger. *Anesthesiology: The Journal of the American*  
734 *Society of Anesthesiologists*, 113(3):678–684, 09 2010.
- 735 [3] Jaap Vuyk, Elske Sitsen, Marije Reekers, et al. Intravenous anesthetics. *Miller’s anesthesia*, 8:858,  
736 2015.
- 737 [4] World Health Organization. Fact file on ketamine. Available at [https](https://www.who.int/medicines/news/20160309_FactFile_Ketamine.pdf?ua=1) :  
738 [//www.who.int/medicines/news/20160309\\_FactFile\\_Ketamine.pdf?ua=1](https://www.who.int/medicines/news/20160309_FactFile_Ketamine.pdf?ua=1), 2015.
- 739 [5] World Health Organization et al. World health organization model list of essential medicines: 21st list  
740 2019. Technical report, World Health Organization, 2019.
- 741 [6] World Health Organization. Letter from the world society of intravenous anaes-  
742 thesia to the ECDD, 8th may 2014. Available at ‘Letters of Support’ [http](http://www.who.int/medicines/areas/quality_safety/36thecddmeet/en/index5.html) :  
743 [//www.who.int/medicines/areas/quality\\_safety/36thecddmeet/en/index5.html](http://www.who.int/medicines/areas/quality_safety/36thecddmeet/en/index5.html), 2014.
- 744 [7] Stewart A Bergman. Ketamine: review of its pharmacology and its use in pediatric anesthesia. *Anes-*  
745 *thesia progress*, 46(1):10, 1999.
- 746 [8] Madhuri. Kurdi, Kaushic. Theerth, and Radhika. Deva. Ketamine: Current applications in anesthesia,  
747 pain, and critical care. *Anesthesia: Essays and Researches*, 8(3):283–290, 2014.
- 748 [9] Steven M. Green, Mark G. Roback, Robert M. Kennedy, and Baruch Krauss. Clinical practice guideline  
749 for emergency department ketamine dissociative sedation: 2011 update. *Annals of Emergency Medicine*,  
750 57(5):449 – 461, 2011.
- 751 [10] P. F. White, J. Schüttler, A. Shafer, D. R. Stanski, Y. Horai, and A. J. Trevor. Comparative Pharmacol-  
752 ogy of the Ketamine Isomers: Studies in Volunteers. *BJA: British Journal of Anaesthesia*, 57(2):197–203,  
753 02 1985.
- 754 [11] Oluwaseun Akeju, Andrew H Song, Allison E Hamilos, Kara J Pavone, Francisco J Flores, Emery N  
755 Brown, and Patrick L Purdon. Electroencephalogram signatures of ketamine anesthesia-induced uncon-  
756 consciousness. *Clinical neurophysiology*, 127(6):2414–2422, 2016.
- 757 [12] Duan Li and George A Mashour. Cortical dynamics during psychedelic and anesthetized states induced  
758 by ketamine. *NeuroImage*, 196:32–40, 2019.
- 759 [13] Francisco J Flores, ShiNung Ching, Katharine Hartnack, Amanda B Fath, Patrick L Purdon, Matthew A  
760 Wilson, and Emery N Brown. A pk–pd model of ketamine-induced high-frequency oscillations. *Journal*  
761 *of neural engineering*, 12(5):056006, 2015.
- 762 [14] Jesus J. Ballesteros, Pamela Huang, Shaun R. Patel, Emad N. Eskandar, and Yumiko Ishizawa. Dynam-  
763 ics of Ketamine-induced Loss and Return of Consciousness across Primate Neocortex. *Anesthesiology*,  
764 132(4):750–762, 04 2020.

- 765 [15] Karen E. Schroeder, Zachary T. Irwin, Matt Gaidica, J. Nicole Bentley, Parag G. Patil, George A.  
766 Mashour, and Cynthia A. Chestek. Disruption of corticocortical information transfer during ketamine  
767 anesthesia in the primate brain. *NeuroImage*, 2016.
- 768 [16] Maya Slovik, Boris Rosin, Shay Moshel, Rea Mitelman, Eitan Schechtman, Renana Eitan, Aeyal Raz,  
769 and Hagai Bergman. Ketamine induced converged synchronous gamma oscillations in the cortico-basal  
770 ganglia network of nonhuman primates. *Journal of neurophysiology*, 118(2):917–931, aug 2017.
- 771 [17] A. U. Nicol and A. J. Morton. Characteristic patterns of EEG oscillations in sheep (*Ovis aries*) induced  
772 by ketamine may explain the psychotropic effects seen in humans. *Scientific Reports*, 10(1):1–10, 2020.
- 773 [18] Jeremy Seamans. Losing inhibition with ketamine. *Nature chemical biology*, 4(2):91–93, 2008.
- 774 [19] Houman Hodayoun and Bitan Moghaddam. NMDA receptor hypofunction produces opposite effects on  
775 prefrontal cortex interneurons and pyramidal neurons. *Journal of Neuroscience*, 27(43):11496–11500,  
776 2007.
- 777 [20] M. M. Kowalski, J. A. Donoghue, M. M. McCarthy, N. J. Kopell, E. K. Miller, and E. N. Brown.  
778 Ketamine anesthesia produces alternating peaks in delta and gamma power in prefrontal and parietal  
779 cortex of macaque monkeys. *Program No. 751.13. 2017 Neuroscience Meeting Planner. San Diego, IL:*  
780 *Society for Neuroscience*, 2017.
- 781 [21] Michelle M McCarthy, Emery N Brown, and Nancy Kopell. Potential network mechanisms mediating  
782 electroencephalographic beta rhythm changes during propofol-induced paradoxical excitation. *Journal*  
783 *of Neuroscience*, 28(50):13488–13504, 2008.
- 784 [22] ShiNung Ching, Aylin Cimenser, Patrick L. Purdon, Emery N. Brown, and Nancy J. Kopell. Thalamo-  
785 cortical model for a propofol-induced  $\alpha$ -rhythm associated with loss of consciousness. *Proceedings of*  
786 *the National Academy of Sciences*, 107(52):22665–22670, 2010.
- 787 [23] Sujith Vijayan, ShiNung Ching, Patrick L. Purdon, Emery N. Brown, and Nancy J. Kopell. Thalamo-  
788 cortical mechanisms for the anteriorization of alpha rhythms during propofol-induced unconsciousness.  
789 *Journal of Neuroscience*, 33(27):11070–11075, 2013.
- 790 [24] Austin E Soplata, Michelle M McCarthy, Jason Sherfey, Shane Lee, Patrick L Purdon, Emery N Brown,  
791 and Nancy Kopell. Thalamocortical control of propofol phase-amplitude coupling. *PLoS computational*  
792 *biology*, 13(12):e1005879, 2017.
- 793 [25] Robert E Kass, Uri T Eden, and Emery N Brown. *Analysis of neural data*, volume 491. Springer, 2014.
- 794 [26] Emery N. Brown, Loren M. Frank, Dengda Tang, Michael C. Quirk, and Matthew A. Wilson. A  
795 statistical paradigm for neural spike train decoding applied to position prediction from ensemble firing  
796 patterns of rat hippocampal place cells. *Journal of Neuroscience*, 18(18):7411–7425, 1998.
- 797 [27] Mark M. Churchland, John P. Cunningham, Matthew T. Kaufman, Justin D. Foster, Paul Nuyujukian,  
798 Stephen I. Ryu, Krishna V. Shenoy, and Krishna V. Shenoy. Neural population dynamics during  
799 reaching. *Nature*, 487(7405):51–56, 2012.
- 800 [28] Leigh R. Hochberg, Mijail D. Serruya, Gerhard M. Friehs, Jon A. Mukand, Maryam Saleh, Abraham H.  
801 Caplan, Almut Branner, David Chen, Richard D. Penn, and John P. Donoghue. Neuronal ensemble  
802 control of prosthetic devices by a human with tetraplegia. *Nature*, 442(7099):164–171, 2006.

- 803 [29] Cynthia A. Chestek, Vikash Gilja, Paul Nuyujukian, Justin D. Foster, Joline M. Fan, Matthew T.  
804 Kaufman, Mark M. Churchland, Zuley Rivera-Alvidrez, John P. Cunningham, Stephen I. Ryu, and  
805 Krishna V. Shenoy. Long-term stability of neural prosthetic control signals from silicon cortical arrays  
806 in rhesus macaque motor cortex. *Journal of Neural Engineering*, 8(4), 2011.
- 807 [30] Jessica Chemali, ShiNung Ching, Patrick L Purdon, Ken Solt, and Emery N Brown. Burst suppression  
808 probability algorithms: state-space methods for tracking EEG burst suppression. *Journal of Neural  
809 Engineering*, 10(5):1–20, 2013.
- 810 [31] Christopher M Bishop. *Pattern recognition and machine learning*. springer, 2006.
- 811 [32] Simo Särkkä. *Bayesian filtering and smoothing*, volume 3. Cambridge University Press, 2013.
- 812 [33] L. R. Rabiner. A tutorial on hidden markov models and selected applications in speech recognition.  
813 *Proceedings of the IEEE*, 77(2):257–286, Feb 1989.
- 814 [34] Z. Liu, J. Huang, and Y. Wang. Classification tv programs based on audio information using hidden  
815 markov model. In *1998 IEEE Second Workshop on Multimedia Signal Processing (Cat. No.98EX175)*,  
816 pages 27–32, 1998.
- 817 [35] Gautham J. Mysore, Paris Smaragdis, and Bhiksha Raj. Non-negative hidden markov modeling of  
818 audio with application to source separation. In Vincent Vigneron, Vicente Zarzoso, Eric Moreau, Rémi  
819 Gribonval, and Emmanuel Vincent, editors, *Latent Variable Analysis and Signal Separation*, pages 140–  
820 148, Berlin, Heidelberg, 2010. Springer Berlin Heidelberg.
- 821 [36] Mohammed Kyari Mustafa, Tony Allen, and Kofi Appiah. A comparative review of dynamic neural  
822 networks and hidden markov model methods for mobile on-device speech recognition. *Neural Computing  
823 and Applications*, 31(2):891–899, 2019.
- 824 [37] Miran Lee, Inchan Youn, Jaehwan Ryu, and Deok Hwan Kim. Classification of Both Seizure and Non-  
825 Seizure Based on EEG Signals Using Hidden Markov Model. *Proceedings - 2018 IEEE International  
826 Conference on Big Data and Smart Computing, BigComp 2018*, pages 469–474, 2018.
- 827 [38] Hojat Ghimatgar, Kamran Kazemi, Mohammad Sadegh Helfroush, and Ardalan Aarabi. An automatic  
828 single-channel EEG-based sleep stage scoring method based on hidden Markov Model. *Journal of  
829 Neuroscience Methods*, 324(June):108320, 2019.
- 830 [39] L G Doroshenkov, V A Konyshov, and S V Selishchev. Classification of Human Sleep Stages Based on  
831 EEG Processing Using Hidden Markov Models. *Biomedical Engineering*, 41(1):25–28, 2007.
- 832 [40] A. Flexer, G. Dorffner, P. Sykacek, and I. Rezek. An automatic, continuous and probabilistic sleep  
833 stager based on a Hidden Markov Model. *Applied Artificial Intelligence*, 16(3):199–207, 2002.
- 834 [41] Andrew H Song, Leon Chlon, Hugo Soulat, John Tauber, Sandya Subramanian, Demba Ba, and  
835 Michael J Prerau. Multitaper infinite hidden markov model for eeg. In *2019 41st Annual Interna-  
836 tional Conference of the IEEE Engineering in Medicine and Biology Society (EMBC)*, pages 5803–5807.  
837 IEEE, 2019.
- 838 [42] Jacob D. Bryan and Stephen E. Levinson. Autoregressive Hidden Markov Model and the Speech Signal.  
839 *Procedia Computer Science*, 61:328–333, 2015.

- 840 [43] David A. Moses, Matthew K. Leonard, Joseph G. Makin, and Edward F. Chang. Real-time decoding  
841 of question-and-answer speech dialogue using human cortical activity. *Nature Communications*, 10(1),  
842 2019.
- 843 [44] J C Kao, P Nuyujukian, S I Ryu, and K V Shenoy. A High-Performance Neural Prosthesis Incorporating  
844 Discrete State Selection With Hidden Markov Models. *IEEE Transactions on Biomedical Engineering*,  
845 64(4):935–945, apr 2017.
- 846 [45] Dror Lederman and Joseph Tabrikian. Classification of multichannel EEG patterns using parallel hidden  
847 markov models. *Medical and Biological Engineering and Computing*, 50(4):319–328, 2012.
- 848 [46] Zhe Chen, Sujith Vijayan, Riccardo Barbieri, Matthew A Wilson, and Emery N Brown. Discrete-  
849 and continuous-time probabilistic models and algorithms for inferring neuronal UP and DOWN states.  
850 *Neural computation*, 21(7):1797–1862, jul 2009.
- 851 [47] James M Mcfarland, Thomas T G Hahn, and Mayank R Mehta. Explicit-Duration Hidden Markov  
852 Model Inference of UP-DOWN States from Continuous Signals. *PLOS ONE*, 6(6), 2011.
- 853 [48] Surya Tokdar, Peiyi Xi, Ryan C. Kelly, and Robert E. Kass. Detection of bursts in extracellular spike  
854 trains using hidden semi-Markov point process models. *Journal of Computational Neuroscience*, 29(1-  
855 2):203–212, 2010.
- 856 [49] Indie C. Rice, Sourish Chakravarty, Pegah Kahali, Jacob Donoghue, Meredith Mahnke, Earl K. Miller,  
857 Oluwaseun-Johnson Akeju, and Emery N. Brown. Detecting bursts in electroencephalography and local  
858 field potential spectrograms using a hidden markov model. *Program No. 523.12. 2018 Neuroscience*  
859 *Meeting Planner. San Diego, IL: Society for Neuroscience*, 2018.
- 860 [50] Diego Vidaurre, Andrew J Quinn, Adam P Baker, David Dupret, Alvaro Tejero-Cantero, and Mark W  
861 Woolrich. Spectrally resolved fast transient brain states in electrophysiological data. *Neuroimage*,  
862 126:81–95, 2016.
- 863 [51] Jeffrey S Rosenthal. *First Look At Rigorous Probability Theory, A*. World Scientific Publishing Company,  
864 2006.
- 865 [52] D. J. Thomson. Spectrum estimation and harmonic analysis. *Proceedings of the IEEE*, 70(9):1055–1096,  
866 Sep. 1982.
- 867 [53] Partha Mitra. *Observed brain dynamics*. Oxford University Press, 2007.
- 868 [54] Hemant Bokil, Peter Andrews, Jayant E. Kulkarni, Samar Mehta, and Partha P. Mitra. Chronux: A  
869 platform for analyzing neural signals. *Journal of Neuroscience Methods*, 192(1):146 – 151, 2010.
- 870 [55] Robert H Shumway and David S Stoffer. *Time series analysis and its applications: with R examples*.  
871 Springer, 2017.
- 872 [56] Arthur P Dempster, Nan M Laird, and Donald B Rubin. Maximum likelihood from incomplete data  
873 via the em algorithm. *Journal of the Royal Statistical Society: Series B (Methodological)*, 39(1):1–22,  
874 1977.

- 875 [57] Leonard E Baum, Ted Petrie, George Soules, and Norman Weiss. A maximization technique occurring in  
876 the statistical analysis of probabilistic functions of markov chains. *The annals of mathematical statistics*,  
877 41(1):164–171, 1970.
- 878 [58] L. Liporace. Maximum likelihood estimation for multivariate observations of markov sources. *IEEE*  
879 *Transactions on Information Theory*, 28(5):729–734, 1982.
- 880 [59] C. F. Jeff Wu. On the convergence properties of the em algorithm. *Ann. Statist.*, 11(1):95–103, 03 1983.
- 881 [60] John D. Cook and Saralees Nadarajah. Stochastic inequality probabilities for adaptively randomized  
882 clinical trials. *Biometrical Journal*, 48(3):356–365, 2006.
- 883 [61] University of Michigan Unit for Laboratory Animal Medicine. *Guidelines on Anesthesia and Analgesia*  
884 *in Non-Human Primates*, 2017.
- 885 [62] Henri GMJ Bertrand, Yvette C Ellen, Stevie O’Keefe, and Paul A Flecknell. Comparison of the effects  
886 of ketamine and fentanyl-midazolam-medetomidine for sedation of rhesus macaques (*macaca mulatta*).  
887 *BMC Veterinary Research*, 12(1):1–9, 2016.
- 888 [63] C Terrance Hawk, Steven L Leary, Timothy H Morris, et al. *Formulary for laboratory animals*. Blackwell  
889 Publishing Professional, 3 edition, 2005.
- 890 [64] Seong-Eun Kim, Michael K. Behr, Demba Ba, and Emery N. Brown. State-space multitaper time-  
891 frequency analysis. *Proceedings of the National Academy of Sciences*, 115(1):E5–E14, 2018.
- 892 [65] A. H. Song, S. Chakravarty, and E. N. Brown. A smoother state space multitaper spectrogram. In  
893 *2018 40th Annual International Conference of the IEEE Engineering in Medicine and Biology Society*  
894 *(EMBC)*, pages 33–36, 2018.
- 895 [66] Hugo Soulat, Emily P. Stephen, Amanda M. Beck, and Patrick L. Purdon. State space methods for  
896 phase amplitude coupling analysis. *bioRxiv*, 2019.
- 897 [67] A. Yousefi, R. S. Fard, U. T. Eden, and E. N. Brown. State-space global coherence to estimate the spatio-  
898 temporal dynamics of the coordinated brain activity. In *2019 41st Annual International Conference of*  
899 *the IEEE Engineering in Medicine and Biology Society (EMBC)*, pages 5794–5798, 2019.
- 900 [68] Michael J Prerau, Ritchie E Brown, Matt T Bianchi, Jeffrey M Ellenbogen, and Patrick L Purdon. Sleep  
901 neurophysiological dynamics through the lens of multitaper spectral analysis. *Physiology*, 32(1):60–92,  
902 2017.
- 903 [69] Emery N Brown, Ralph Lydic, and Nicholas D Schiff. General anesthesia, sleep, and coma. *New England*  
904 *Journal of Medicine*, 363(27):2638–2650, 2010.
- 905 [70] Michael J Prerau and Patrick L Purdon. A probabilistic framework for time-frequency detection of  
906 burst suppression. In *2013 6th International IEEE/EMBS Conference on Neural Engineering (NER)*,  
907 pages 609–612. IEEE, 2013.
- 908 [71] Patrick L Purdon, Eric T Pierce, Eran A Mukamel, Michael J Prerau, John L Walsh, Kin Foon K  
909 Wong, Andres F Salazar-Gomez, Priscilla G Harrell, Aaron L Sampson, Aylin Cimenser, et al. Elec-  
910 troencephalogram signatures of loss and recovery of consciousness from propofol. *Proceedings of the*  
911 *National Academy of Sciences*, 110(12):E1142–E1151, 2013.

- 912 [72] Jonathan Cannon, Michelle M McCarthy, Shane Lee, Jung Lee, Christoph Börgers, Miles A Whitting-  
913 ton, and Nancy Kopell. Neurosystems: brain rhythms and cognitive processing. *European Journal of*  
914 *Neuroscience*, 39(5):705–719, 2014.
- 915 [73] Michelle M McCarthy, ShiNung Ching, Miles A Whittington, and Nancy Kopell. Dynamical changes  
916 in neurological diseases and anesthesia. *Current Opinion in Neurobiology*, 22(4):693 – 703, 2012. Mi-  
917 crocircuits.
- 918 [74] Yumiko Ishizawa, Omar J Ahmed, Shaun R Patel, John T Gale, Demetrio Sierra-Mercado, Emery N  
919 Brown, and Emad N Eskandar. Dynamics of propofol-induced loss of consciousness across primate  
920 neocortex. *Journal of Neuroscience*, 36(29):7718–7726, 2016.
- 921 [75] Carlos A. Zarate Jr, Jaskaran B. Singh, Paul J. Carlson, Nancy E. Brutsche, Rezvan Ameli, David A.  
922 Luckenbaugh, Dennis S. Charney, and Husseini K. Manji. A Randomized Trial of an N-methyl-  
923 D-aspartate Antagonist in Treatment-Resistant Major Depression. *Archives of General Psychiatry*,  
924 63(8):856–864, 08 2006.
- 925 [76] Giacomo Salvatore and Jaskaran B. Singh. Ketamine as a fast acting antidepressant: Current knowledge  
926 and open questions. *CNS Neuroscience & Therapeutics*, 19(6):428–436, 2013.
- 927 [77] Thomas R Insel. Rethinking schizophrenia. *Nature*, 468(7321):187–193, 2010.
- 928 [78] Joel Frohlich and John D Van Horn. Reviewing the ketamine model for schizophrenia. *Journal of*  
929 *Psychopharmacology*, 28(4):287–302, 2014. PMID: 24257811.
- 930 [79] Dimitri P Bertsekas. *Constrained optimization and Lagrange multiplier methods*. Academic press, 2014.